Version 6.0
January 22, 2021

Exploring the Great Pyramid: Detector Technical Design Report with Stand-Alone Monte Carlo Simulations

Sophie Dukes, Omar Shohoud, Tabitha Welch

Abstract

Cosmic-ray muon imaging has been used to non-destructively examine the Pyramids of Khufu and Khafre on the Giza Plateau; the EGP project will continue this line of research by undertaking a full tomographic scan of the former and by doing so will increase the sensitivity of the technique by upwards of two orders of magnitude. For this purpose, a muon telescope using triangular (vernier) detector cells far outperforms one with rectangular cells, providing an angular and positional RMS improvement by a factor of 4 for the same cost per unit area. A refinement algorithm was developed to handle tracks that produce secondaries. The triangular detector yields a positional resolution for a back-projection to the center of the pyramid of less than 20 cm, ensuring that a feature large enough to be of significance will still be seen by the telescope. This method is shown to be able to accurately and precisely reconstruct tracks of muons that pass through the King's Chamber, Queen's Chamber, and Grand Gallery.

Contents

1 Introduction

The construction of the Great Pyramid, the oldest of the Seven Wonders of the ancient world and the only one left standing, still stirs debate among archaeologists. Many mysteries pertaining to its construction still remain. This begs the question: does the inside of the pyramid contain something of interest, something that could explain how the ancient Egyptians built these marvels?

Such a question has been difficult to answer, as excavating the pyramids would have dramatic economic and cultural consequences for Egypt. However, the invention of muon tomography by Alvarez et al.—using cosmic-ray muons to scan the inside of the pyramid—may be the solution. This paper uses physics simulation engines to investigate the detectors to be used by the Exploring the Great Pyramid (EGP) Mission, a collaboration between Fermilab, the University of Chicago, the University of Virginia, and the Oriental Institute.

1.1 Historical Background

In 1970, L. Alvarez et al. published an article in *Science* that detailed their scan of Khafre's pyramid using cosmic-ray muon radiography [1]. This experimental setup involved placing two 1.8-meter square spark chambers in Khafre's Belzoni Chamber, which lies near the center of the pyramid's base. Alvarez' main goal was to locate previously undiscovered chambers; this was driven by the apparently stark differences in internal complexity

between this pyramid and the Great Pyramid, its predecessor. While the study found no such chambers, the technique itself was shown to be successful.

Alvarez' exploration was followed in 2017 by the ScanPyramids collaboration, whose study of the Great Pyramid identified a previously unknown void above the Grand Gallery [2]. This void, which is a minimum of 30 m in length and has a cross-section like that of the Grand Gallery, is the first major structure to be discovered within the pyramid since the 1800s. The ScanPyramids group also used muon radiography as their primary tool.

1.2 Motivation

Despite the considerable success of these projects, numerous open questions remain regarding the Great Pyramid's interior and construction. Unlike previous experiments, EGP proposes to apply fully three-dimensional tomographic imaging techniques; this will allow us to differentiate not only void from stone, but also much smaller variations in density. Moreover, the EGP detectors will possess about 100x the area of those used by the ScanPyramids team, yielding appreciably higher resolution. The combination of these factors should provide insight on the nature of the ScanPyramids void, the techniques used to build the pyramid, and the presence of additional unknowns within its structure.

1.2.1 Possibility of a Second King's Chamber

Micro-gravity imaging has revealed curious density variations near the pyramid's peak [10]. These variations suggest the existence of another King's Chamber (henceforth referred to as the Phantom Chamber). Its existence was simulated in our Monte Carlo to test the detectors capability to spot this unknown.

2 The Great Pyramid and Giza Plateau

Here, we discuss the geography of the Giza Necropolis and describe the development of a highly detailed model of the Great Pyramid's interior. The latter will be incorporated into future simulations, which will allow us to more accurately predict the performance of the final detector design.

2.1 The Great Pyramid Model

For the past two months, a CAD model of the interior of the Great Pyramid of Giza has been under development to define where there are known voids and material changes within the pyramid and to provide a baseline to compare with the tomography results. Illustrations of this model are shown in Figure 1. The initial idea was to add in a few details to an existing model, but to save the time of checking the accuracy of the existing model, a new one was begun. Using primarily the plans from Randaldi's *L'architettura Delle Piramidi Menfite* from 1965, a Fusion 360 model was created. One of the biggest challenges was drawing up the Relieving Chambers above the King's Chamber (see Figure 2). This was done by scaling an image of the profiles of the granite blocks that support the relieving chambers and using the loft tool to create bodies from those profiles. The excavation sites, the well shaft tunnel, the North air shaft from the King's Chamber, and Caliph al Ma'mun's forced entry were all areas for which the plans lacked detailed information. Using a similar

technique to how the granite blocks were created, images of the outlines of these areas were scaled up and traced to create the voids. Fewer details were included below the ground level, as those areas will not be measured or studied. The next steps include fleshing out the exterior of the pyramid and creating a smaller, simplified model to practice with.

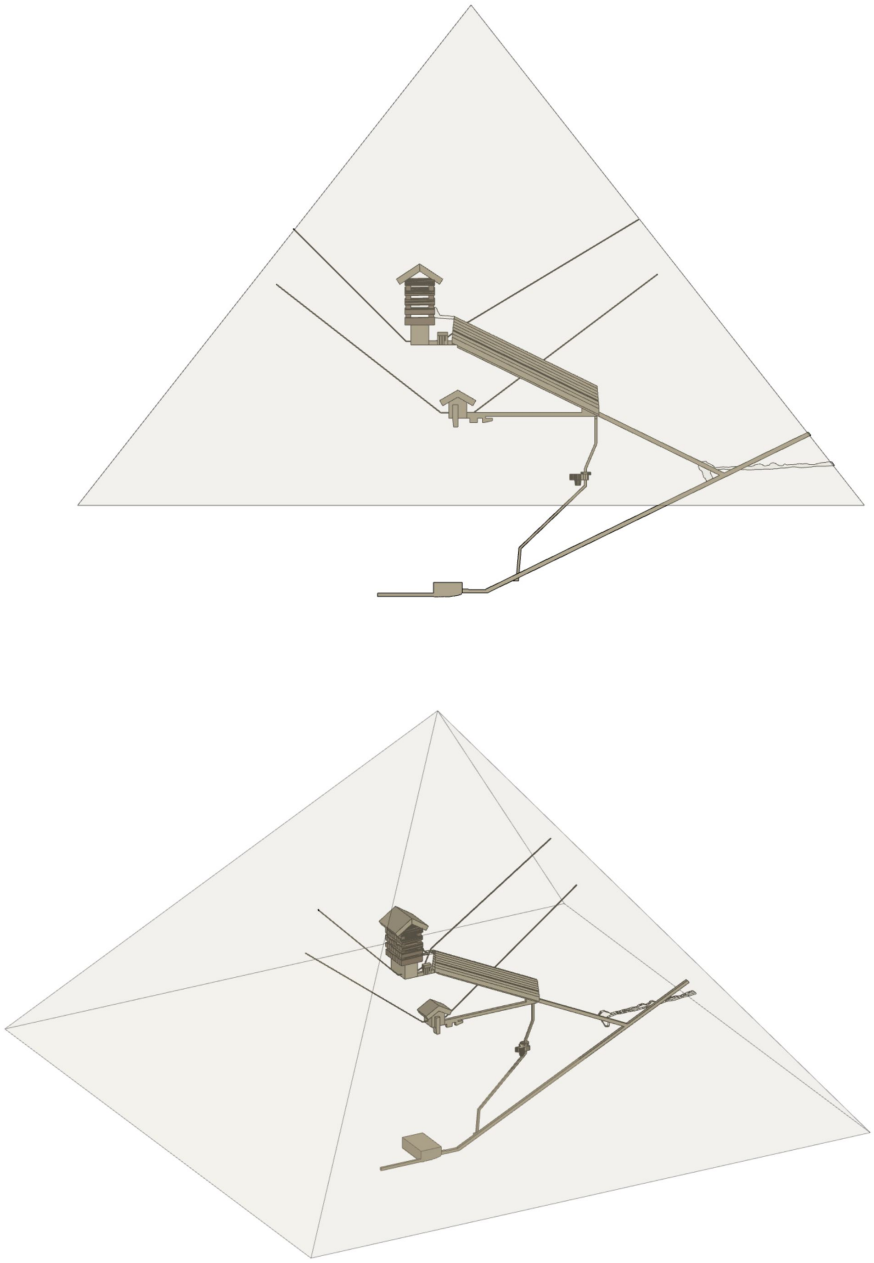

Figure 1: Images of the full CAD model of Khufu's Pyramid.

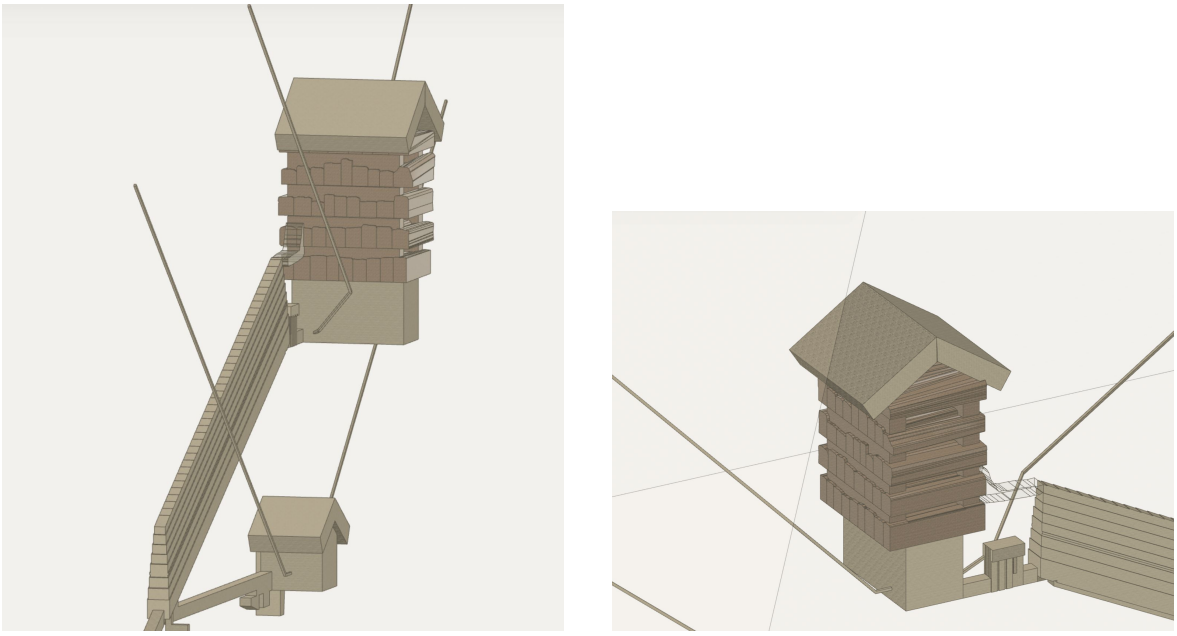

Figure 2: The Grand Gallery (left) and King's Chamber with additional relieving chambers (right) as incorporated into the CAD model.

2.2 Giza Plateau - Geography

The geography in the pyramid's vicinity provides insight regarding possible detector placements. Below is a plan view of the pyramid and surrounding features, as well as suggested detector locations.

There are a few obstructions surrounding the pyramid, namely on the southern side; the boat museum and other buildings may cause interference. The western and northern sides are relatively unobstructed, however, providing us with two adjacent sides with a sufficient view to provide a precise tomographic reconstruction.

Below are images of the pyramid and surroundings taken using Google Earth.

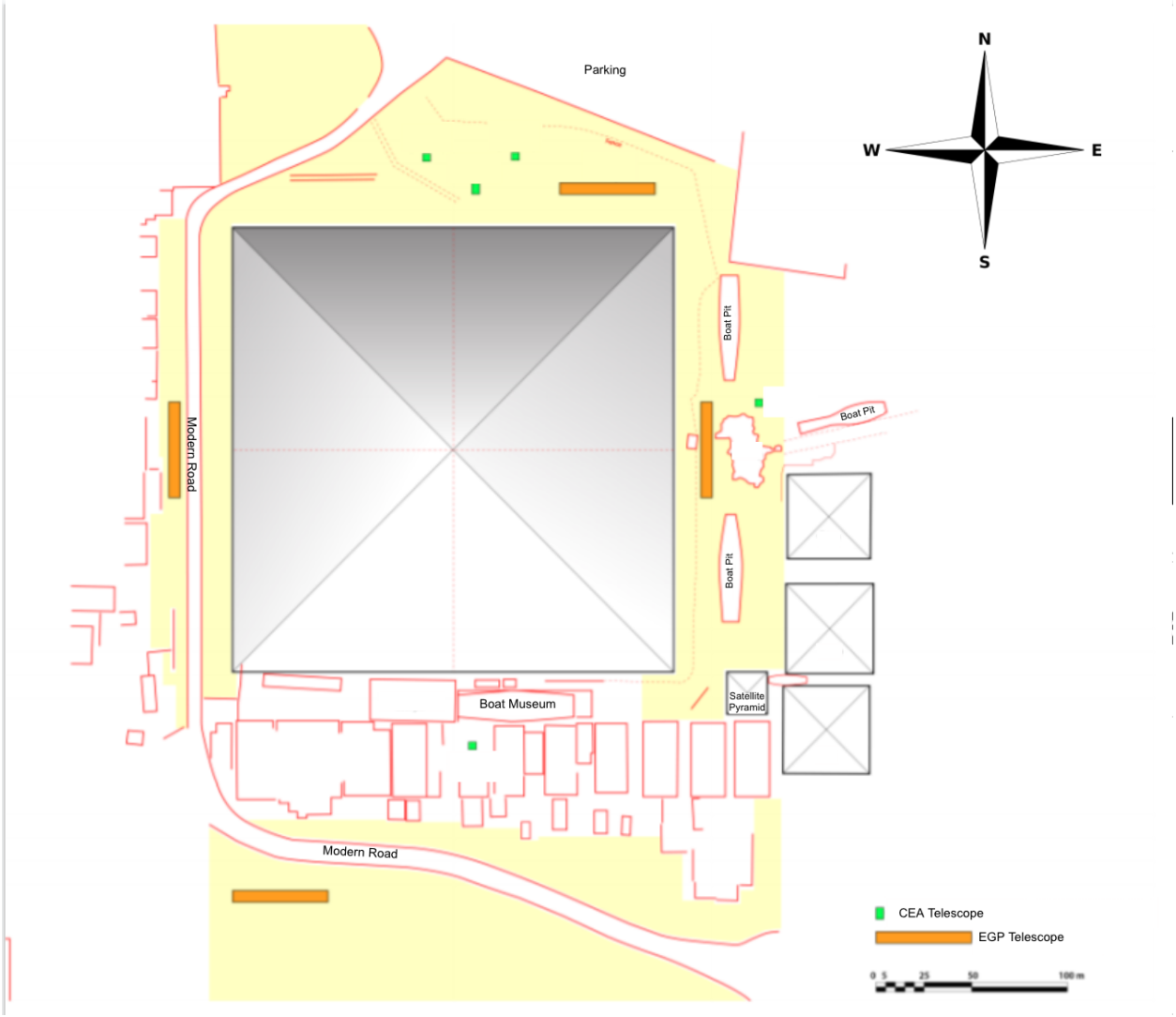

Figure 3: Plan view of the pyramid and surroundings, with significant features and suggested detector placements labeled.

Figure 4: Ground view of the west side of the pyramid (looking north), near the face.

Figure 5: Ground view of the west side of the pyramid (looking north), on the road.

Figure 6: Ground view of the east side of the pyramid (looking north), near the face.

Figure 7: Ground-side view of the south side of the pyramid (looking east), near the face.

Figure 8: Ground-front view of the south side of the pyramid (looking north), on the road.

3 Detector Configuration

The detector arrangement is shown in Figure 9.

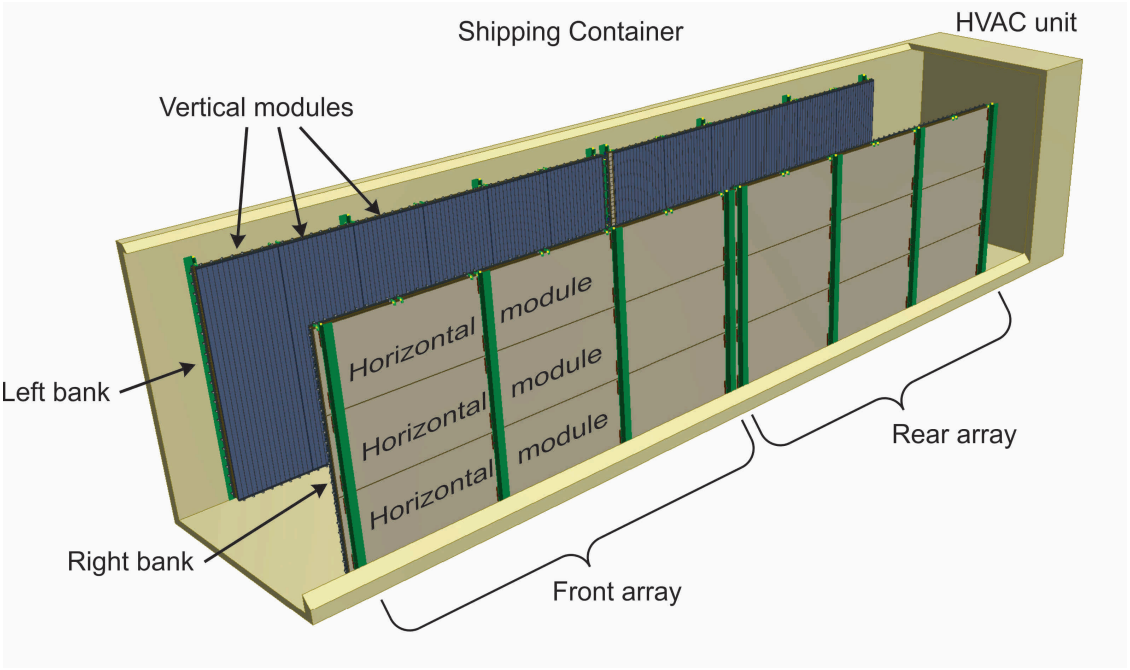

Figure 9: Diagram of detectors in cargo container.

The configuration consists of two banks, separated by 2 m, each containing two detectors: one with horizontal modules and one with vertical modules. Each module has a width of 80 cm, and a total of 40 counters. For the rectangular detectors, each counter has a width of 2 cm, creating a 2 cm x 2 cm grid in each bank. For the vernier detectors, the triangular face of each module has a base of 4 cm and a height of 2 cm (their arrangement will be detailed in Section 5.2), covering the same area with the same number of modules as their rectangular counterparts. Horizontal modules have a length of 4.8 m, while vertical strips have a length of 2.4 m. Conversely, there are 12 vertical modules per bank, with only 6 horizontal per bank.

The cargo container holding these modules has 5 mm thick aluminum walls. Four cargo containers will be stacked to form a 2x2 array, creating a total detector area of 92.16 m^2.

4 Coordinate System

The coordinate system used in our simulations is shown in Figures 10, 11, and 12. Figures 10 and 11 include plan and elevation views of the pyramid, with proposed detector setup for reference. We make use of both global and local coordinates; the global Cartesian coordinates are designated (X,Y,Z), and their polar counterparts, used for describing muon trajectories, are (θ,ϕ). The global coordinates' origin is located at the center of the pyramid's base, and the X axis points east, while the Y axis points north and the Z axis points upwards. The local Cartesian coordinates we use are (u,v); they span a given detector plane, with the origin at the bottom left corner of that plane from the perspective facing the pyramid.

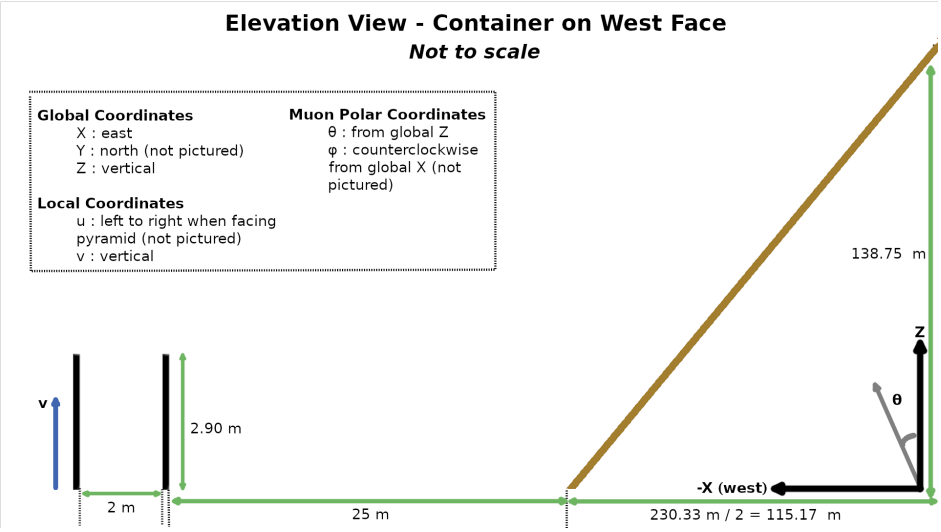

Figure 10: Elevation view of coordinate system used for all simulations, with the pyramid for reference. We define both local coordinates (u,v) - to describe locations on a given detector plane - and global coordinates (X,Y,Z), as well as polar coordinates (θ,ϕ) to describe muon trajectories. The origin of the global coordinates is at the center of the pyramid's base, while the origin of the local coordinates is at the corner of the relevant detector plane (see Figure 12).

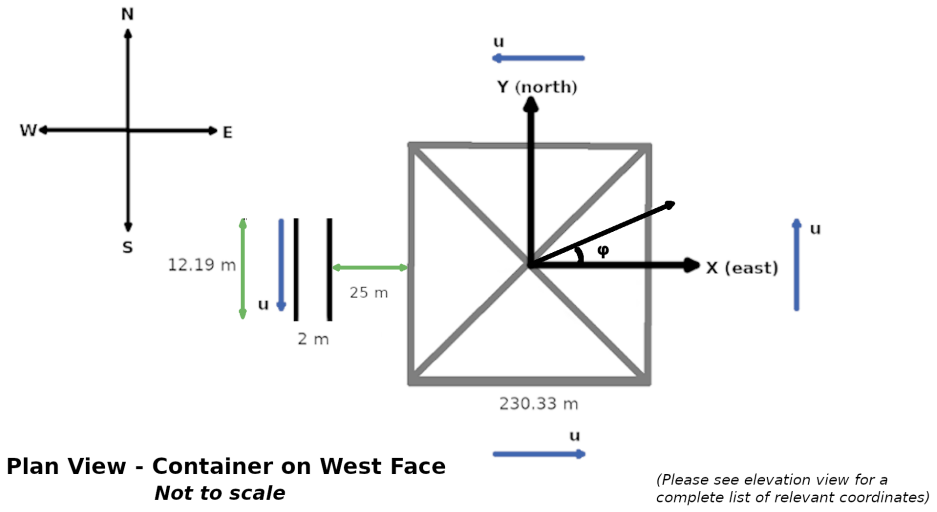

Figure 11: Plan view of the coordinate system. The global X axis points east, while the global Y axis points north; Z points upwards out of the page. The orientation of the local u axis varies by specific container placement, as shown, and the local v axis always points up.

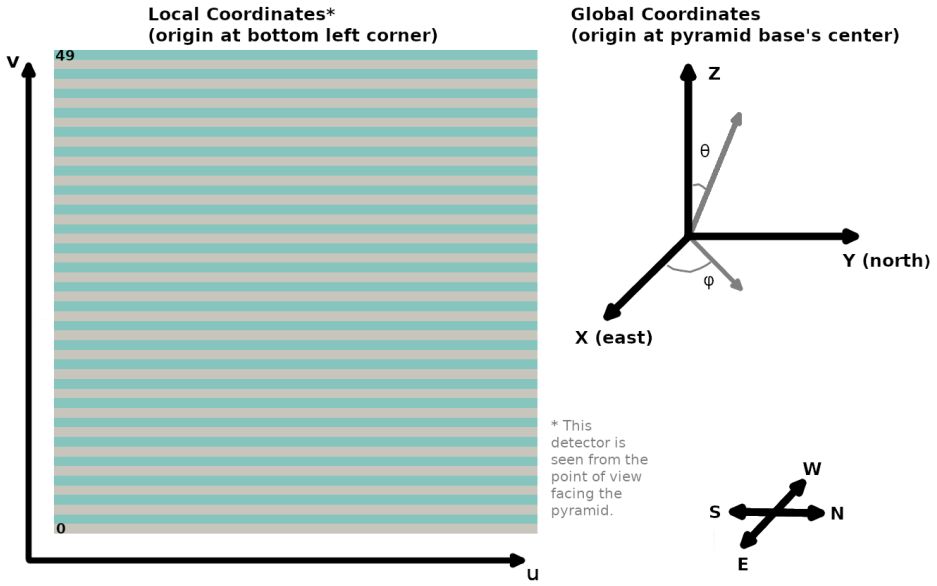

Figure 12: Detailed coordinate system.

5 Simulation Parameters

We developed two toy models - one based on a rectangular scintillator design, and the other based on a triangular or vernier design. The former was simulated with the GEANT4 toolkit [5, 6]; the latter used G4beamline [7]. Supporting analysis was performed in Root, and visualizations of the rectangular design were produced with Paraview. The primary objectives of this study were to investigate the positional and angular resolution needed in light of multiple scattering effects, and to determine which of the two strip designs best fulfilled these requirements.

5.1 Rectangular Model

As shown in Figure 13, the rectangle-based toy model consists of two 1 m x 1 m detectors. These correspond to the detectors on the two walls of the cargo container discussed above, so there is a 2 m gap between them. Each detector is composed of two planes of 50 rectangular scintillator strips, and each strip has dimensions of 2 cm x 2 cm x 1 m. In each detector, one set of strips is vertical and the other is horizontal, which yields a set of u and v coordinates for every hit (see section 8.1 for details). These detectors sit in a vacuum; no container walls, electronics, or fibers are included in the simulation.

G4ParticleGun, GEANT's simple built-in particle gun, serves as the muon source for the model. This gun produces one muon at a time, with exactly the same initial momentum and position each time. In a given run of the simulation, a pre-determined number of these identical muons are fired at the detectors, and information about their energy deposition in the scintillator strips is recorded (see below).

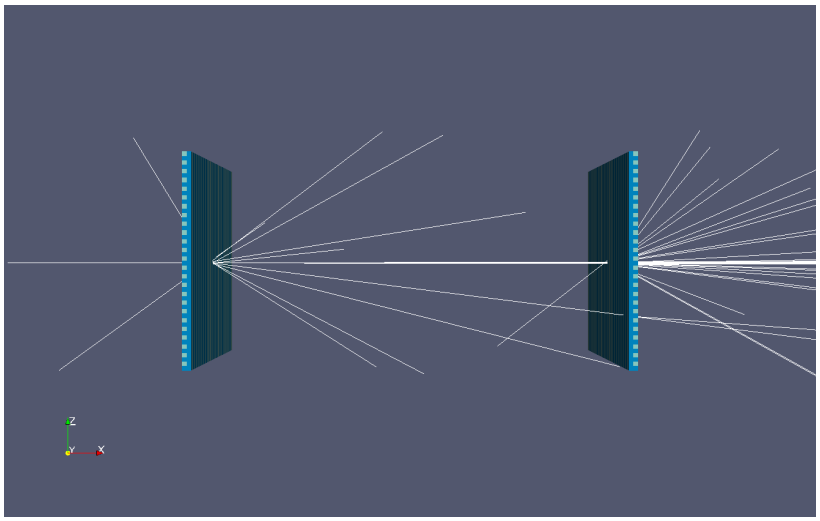

Figure 13: The simulation contains two detectors, each consisting of two 1 m x 1 m scintillator planes and each plane composed of 50 2 cm x 2 cm x 1 m strips; there is a 2 m gap between the first and second detectors. In the above visualization, tracks from 100 4 GeV muons and all of their associated secondaries are shown, each muon beginning to the left of detector 1. (Note: the secondary particle removal discussed in section 5.1.1 applies only to the concrete volume and is therefore not relevant here.)

For studies involving multiple-scattering effects from the pyramid itself, we added a concrete block 25 m upstream of the detectors to simulate the pyramid. This is shown in Figure 14. We varied the thickness of this block in order to represent potential voids at different depths inside the pyramid; a 115-m block corresponded to a hypothetical chamber at the pyramid's center and was therefore the greatest thickness of interest (see Figure 10).

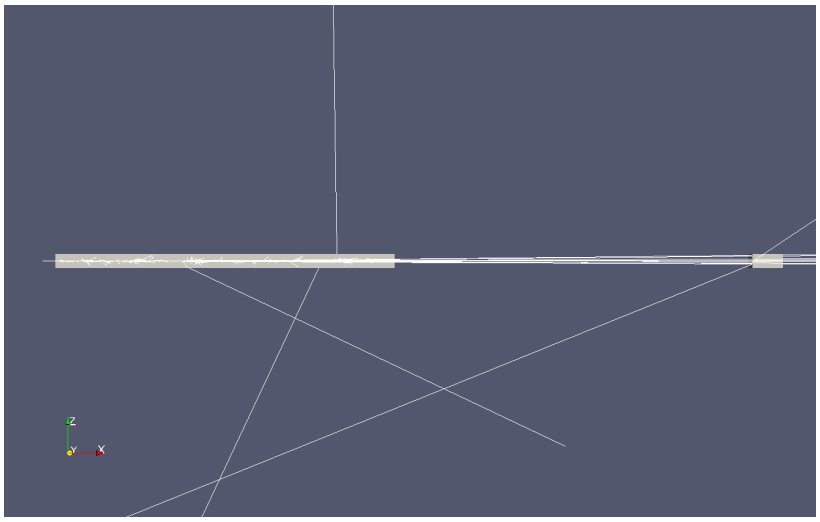

Figure 14: A concrete block that served as a pyramid dummy was later added 25 m upstream of the detectors. The width and height of this block matched that of the detectors; its length was varied between 1 and 115 m. In this visualization, the block is 25 m long and is shown with tracks from 10 50 GeV muons and their secondaries. No secondaries that were generated in the concrete with energy greater than 10 MeV are shown (see section 5.1.1 for details). The detector is shown in gray at the right side of the image.

5.1.1 Removing Tracking of Secondary Particles to Improve Simulation Speed

Particularly with the addition of the concrete block discussed above, simulation speed became a major concern. Since most secondary particles produced inside the concrete have no impact whatsoever on the results, it is completely unnecessary to track them for our purposes. So, a cut was implemented within the concrete volume that resulted in all secondaries below the threshold energy being killed immediately upon creation. Table 1 details the timing results from these changes. For most runs with concrete, a 10-MeV cutoff was used.

Concrete Thickness (m)	All Secondaries	10 MeV Secondary Cutoff in Concrete	10 GeV Secondary Cutoff in Concrete
50	User=408s Real=1830s Sys=322s	User=93.1s Real=424s Sys=76.8s	User=36.7s Real=147s Sys=31.2s
25	User=227s Real=954s Sys=178s	User=48.0s Real=199s Sys=40.6s	User=18.5s Real=72.6s Sys=15.9s
10	User=86.2s Real=360.s Sys=67.4s	User=19.0s Real=82.5s Sys=16.0s	User=7.54s Real=32.3s Sys=6.64s
5	User=45.0s Real=183s Sys=35.5s	User=9.50s Real=42.5s Sys=7.98s	User=4.03s Real=15.9s Sys=3.35s

Table 1: Raw timing data from runs of 1,000 50-GeV muons with various concrete thicknesses. Introducing a 10-MeV cut on secondaries generated inside the concrete resulted in a 4x speedup over keeping all secondaries, while a 10-GeV cut, which essentially eliminated all concrete-generated secondaries, further increased the simulation's speed by about another factor of three. Note: in the above, "real" refers to the total time elapsed from the simulation's start to its finish (i.e., wall clock time). "User" and "sys" refer to CPU time spent outside and inside the Unix kernel, respectively; their sum represents the total CPU time.

5.2 Vernier Model

This simulation replaced the rectangular scintillator cells with triangular ones to utilize multiple hits and $\frac{dE}{dx}$ in the algorithm. The face of each cell had 4 cm base and 2 cm height, and the length of each cell was 2.52 m. Each cell had a cylindrical hole running along the length of the prism, with diameter 1.2 mm, located 8.5 mm above the base of the triangle. Each plane was 2.52 m x 2.52 m and contained 126 cells, arranged as shown in Figure **??** to form the plane.

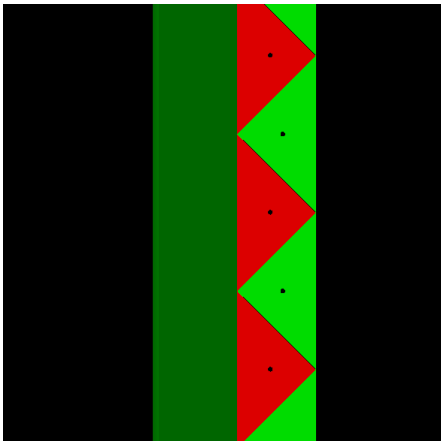

Figure 15: Zoomed-in plan view of detector planes 1 and 2. Cells are isosceles triangular prisms with 40 mm base and 20 mm height, and 2.52 m in length. Each cell has a hole 10 mm above the base to simulate the lack of $\frac{dE}{dx}$ in the scintillator due to the wavelength-shifting fiber

Each bank consisted of 2 detector planes, rotated 90 degrees relative to one another to track Z- and Y-coordinates, respectively. There were 2 banks in total, separated by 2 m.

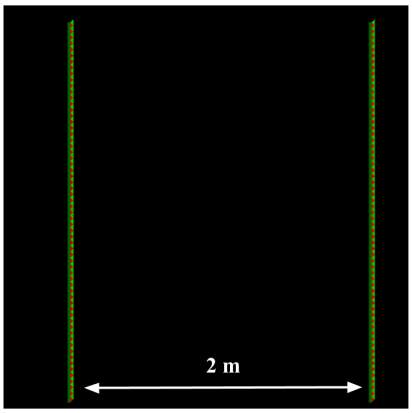

Figure 16: Plan view of all 4 detector planes. There are two banks, each of which has two planes that are rotated 90° with respect to one another, and are otherwise identical in construction and configuration. The banks are separated by 2 m.

Muons were fired every 10 ns, and were positioned and angled such that they hit both banks. In some cases, this required a displacement in the second detector bank.

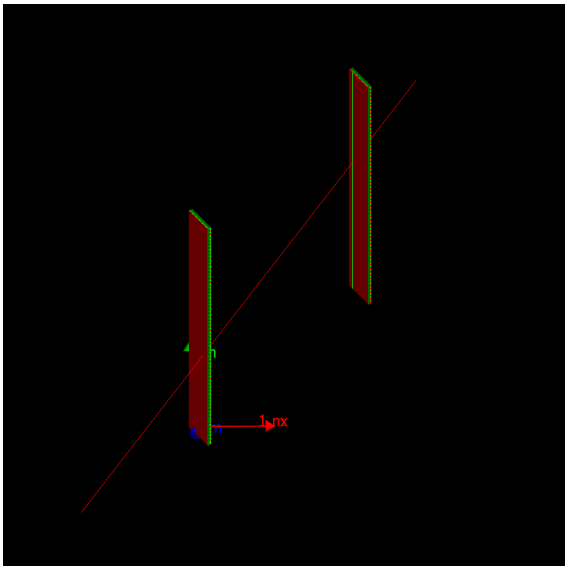

Figure 17: Plan view of muons at $\theta, \phi = 45°$ with displaced back detector bank, entering from the left.

The algorithm used to determine θ, ϕ, as well as x, y, and z position on each detector plane was as follows.

For each collision within a detector cell, the time, detector cell number, and energy deposited were recorded from the simulation. The energy deposition was converted to photoelectrons with a conversion rate of 25 PE/MeV, and a gaussian smearing with RMS $\frac{1}{\sqrt{50}}$. After the conversion, if the energy deposited produced a signal that was below the threshold of 2.5 PE, the collision was discarded.

Collisions in the same plane were grouped in 3 ns "time slices." In each time slice, collisions were removed if they were not contiguous around the most energetic collision. Time slices were connected between planes to form a muon track. Time slices between planes in the same bank were within 3 ns of one another, while time slices in different banks were between 5 and 15 ns apart.

Once these time slices were grouped, each time slice was cut to only two cell hits with a refinement algorithm outlined in Section 6.2. To determine a y- and z-coordinates for each bank, the energy-weighted positional mean was taken:

$$\frac{E_1 P_1 + E_2 P_2}{E_1 + E_2},$$

where E and P are the energy readout and center position for their respective detector cells. An x-coordinate for each plane was determined with the following equations.

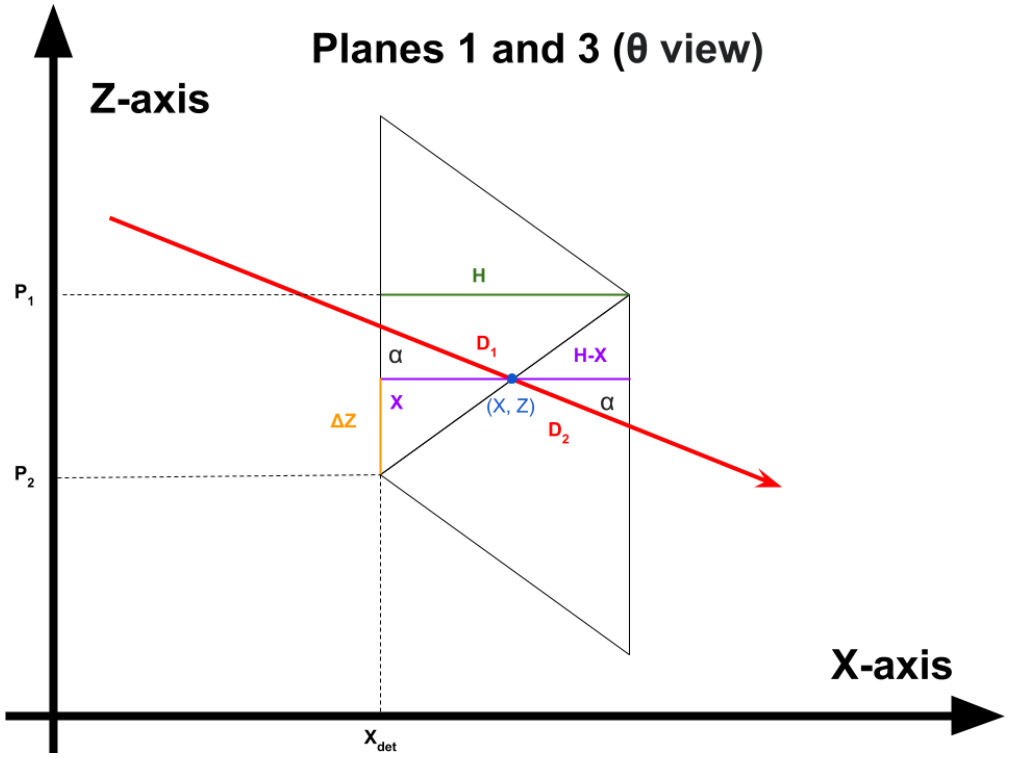

Figure 18: Diagram of muon track in vernier-cell detector with labels.

Since energy deposited is proportional to path length, we can find X and Z with the equations

$$X = X_{det} + \frac{E_1 H}{E_1 + E_2} \tag{1}$$

$$Z = P_2 + \Delta Z = \frac{E_1 P_1 + E_2 P_2}{E_1 + E_2} \tag{2}$$

Trigonometry was then used to determine the azimuthal and zenith angles (ϕ and θ, respectively), and to fully reconstruct the muon path vector.

6 Multiplicity

Appropriately reconstructing the position and angle of an incident muon depends heavily on the number of hits it generates in the detector planes. We therefore investigated the correlation between the hit multiplicity of a particle and its angle with respect to the detector.

6.1 Rectangular Model

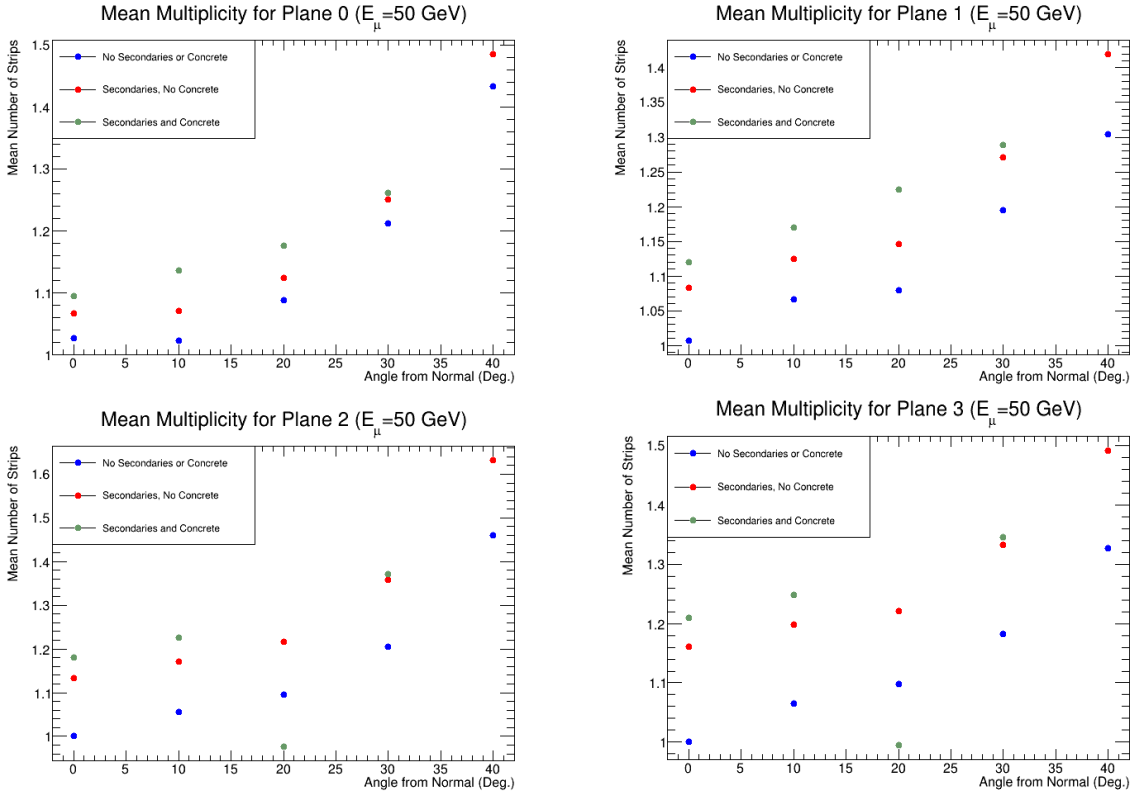

Figure 19: The mean hit multiplicity for each of the four detector planes, plotted as a function of incident angle. Each run consisted of 10,000 50-GeV muons, which were scanned across a full cell width (2 cm).

For the rectangular scintillator model, the analysis described above was repeated for three different cases: 1.) allowing no secondary particles (even from interactions in the scintillator) and including no concrete, 2.) allowing secondary particles, but including no concrete, and 3.) including both secondaries (up to the cut described in 5.1.1) and concrete. All data used an incident muon energy of $E_\mu = 50$ GeV, and for this study only, the detector size was increased to 3 m x 3 m to accommodate the angles of interest. The size of the individual scintillator strips, as well as the 2-m gap between the first and second banks, remained unchanged. For the trials involving concrete, the block was positioned at the same angle as the muon beam - i.e., for every run, the particles passed through exactly 25 m of concrete, regardless of their angle with respect to the detectors. Unlike the other studies discussed here, the beam was scanned across a full cell width during each run.

Figure 19 shows the mean multiplicity in each individual plane for the three scenarios considered. All four planes show a consistent increase in multiplicity as incident angle increases. The trend is present even for runs with no secondary particles, which implies that it stems mainly from the geometry of the situation.

One simple approach to calculating hit position entails using only those events that result in a single hit per plane and rejecting the remainder. We refer to this as the "singles cut." Table 2 and Figure 20 depict the percentage of events that pass this cut in the three simulation scenarios discussed above. For angles close to normal, the majority of events survive; however, there is a sharp decrease in surviving events for wider angles. This is

consistent with the multiplicity trends for individual planes (see above). So, while the singles cut is useful for near-normal incidence, it should not be applied to events with arbitrary angles. For the latter, a weighted mean or clustering algorithm is necessary. In section 8.1, only normal muons were used, and the singles cut was applied.

Angle (Deg.)	No Secondaries	Secondaries, No Concrete	Secondaries and 25 m. Concrete
0	96.81	75.080	71.99
10	90.73	68.55	62.87
20	78.11	59.80	37.99
30	65.54	49.12	29.56
40	51.99	39.12	—

Table 2: For each of the above three situations, the percentage of events that survive if we limit to only one hit per plane in all four planes. This is the "singles cut." Here, "angle" refers to the amount by which both θ and ϕ differ from normal incidence.

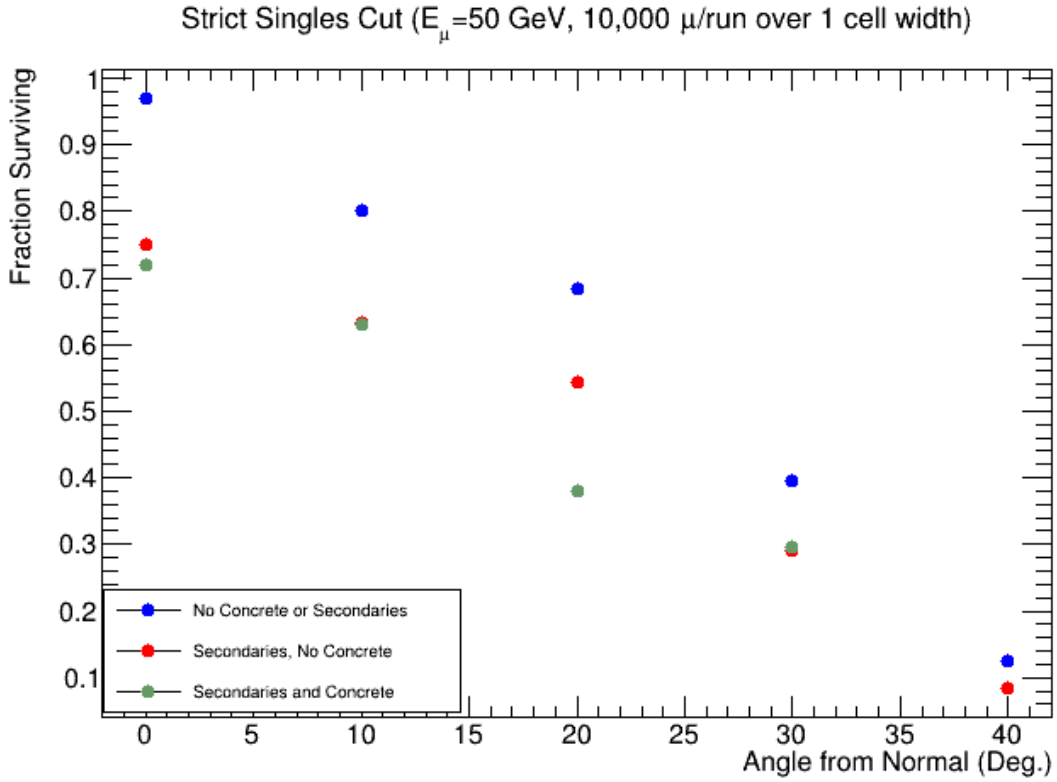

Figure 20: The fraction of events that pass the singles cut, plotted as a function of angle from normal incidence. The sharp decrease in surviving events as angle widens indicates that the singles cut is not appropriate for most muons of interest.

6.2 Vernier Model

The multiplicity (number of cells hit per plane) of a muon track largely depends on the track's angle and position along the base of the cell. Due to the triangular geometry, the trends are periodic, as expected. This causes the angular RMS to vary with position along the cell. To get an accurate figure for the detector's angular RMS, the position of the muons was scanned along the base of the triangle for each trial. Muons were fired at intervals of 0.4 mm across a range of 40 mm, spanning a full cell base.

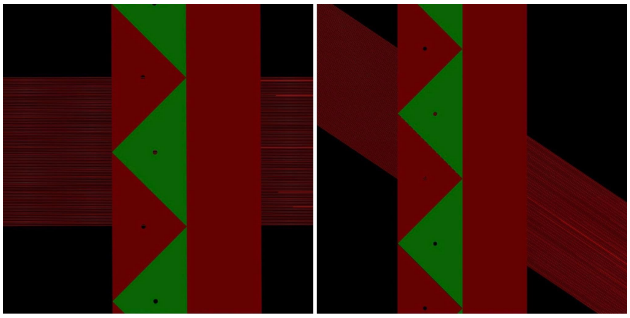

Figure 21: Muons at normal incidence and $\theta, \phi = 30°$ scanning along cell base.

Multiplicity also varies as muons produce secondaries. Investigating the data regarding secondary collisions gives insight into refining time slices so that only muon collisions remain. For these plots, 0 mm indicates the center of the red triangle, moving up in Figure 21.

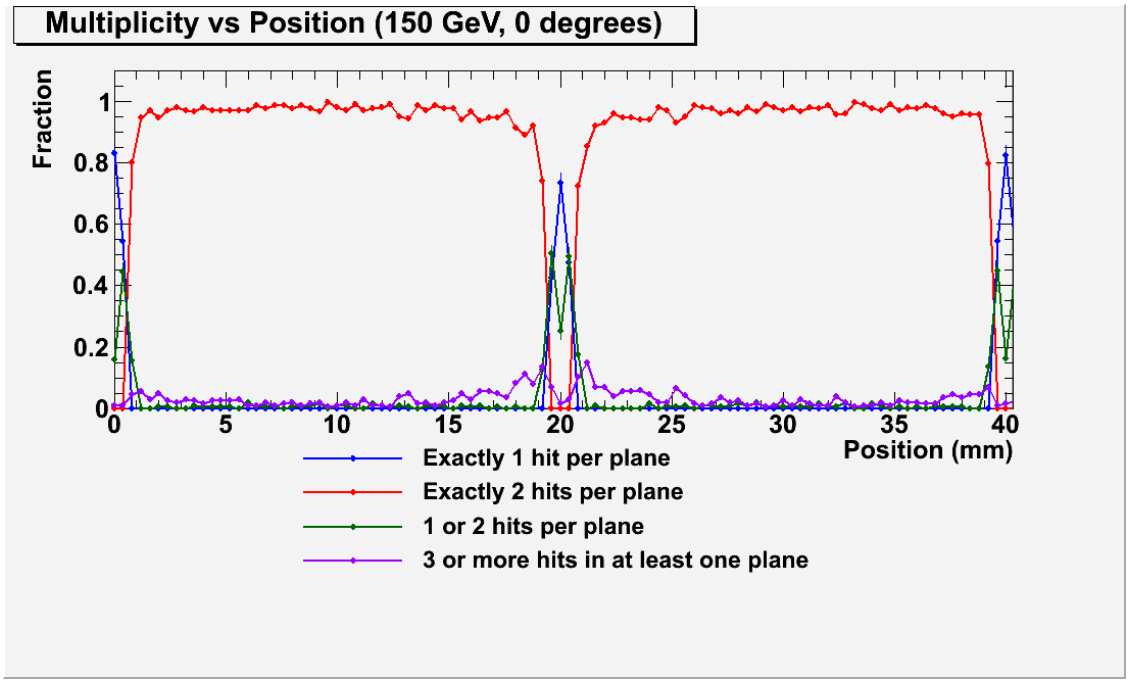

Figure 22: Multiplicity vs Position along cell for muons at normal incidence (Linear Scale).

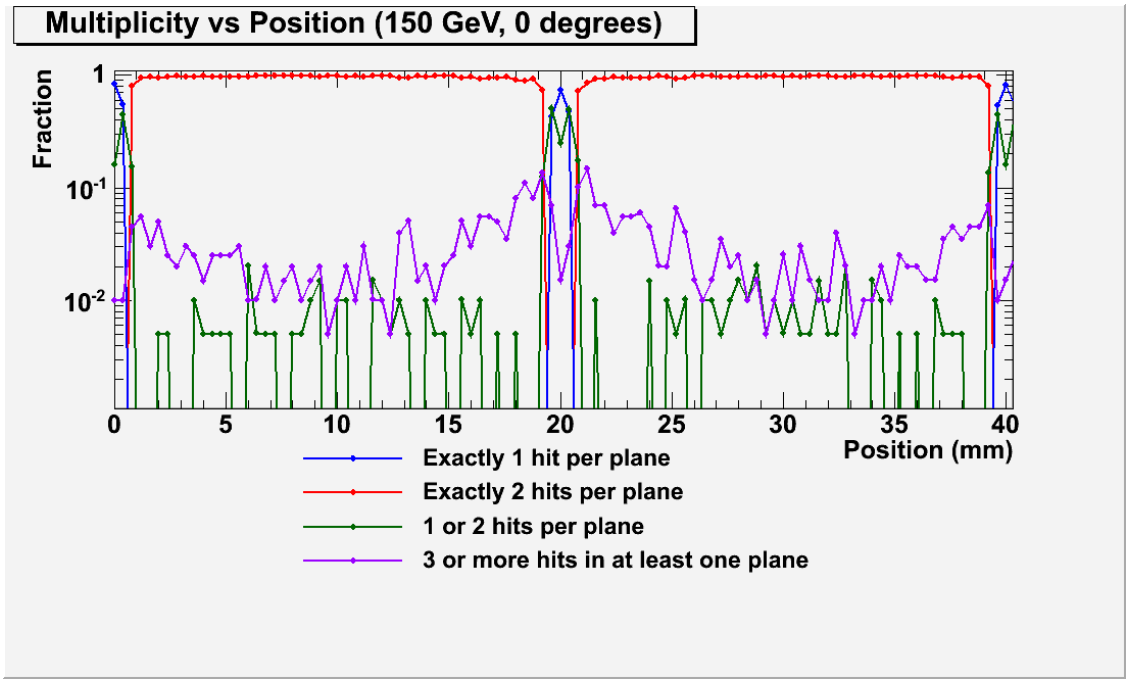

Figure 23: Multiplicity vs Position along cell for muons at normal incidence (Log Scale).

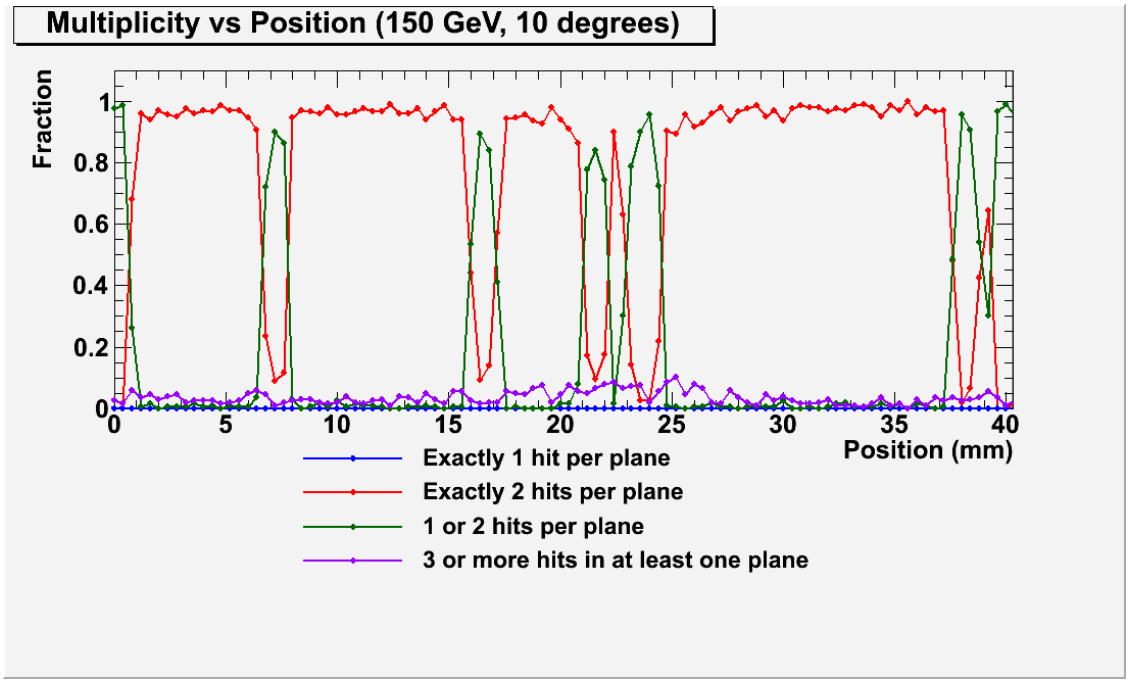

Figure 24: Multiplicity vs Position along cell for muons at $\theta, \phi = 10°$ (Linear Scale).

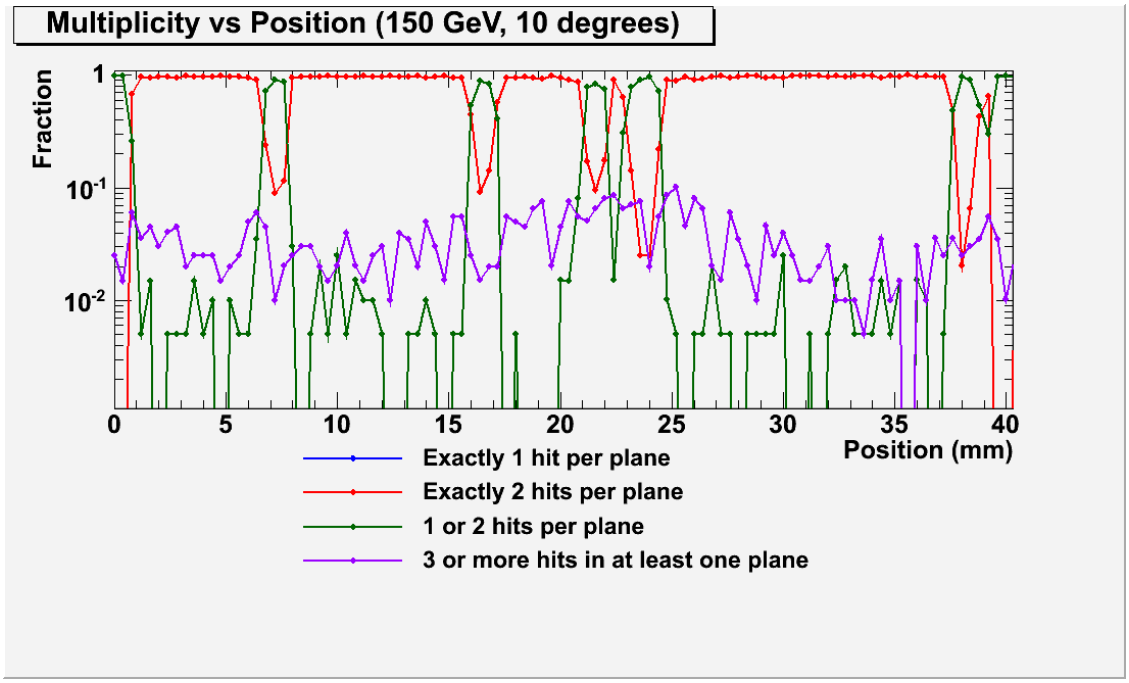

Figure 25: Multiplicity vs Position along cell for muons at $\theta, \phi = 10°$ (Log Scale).

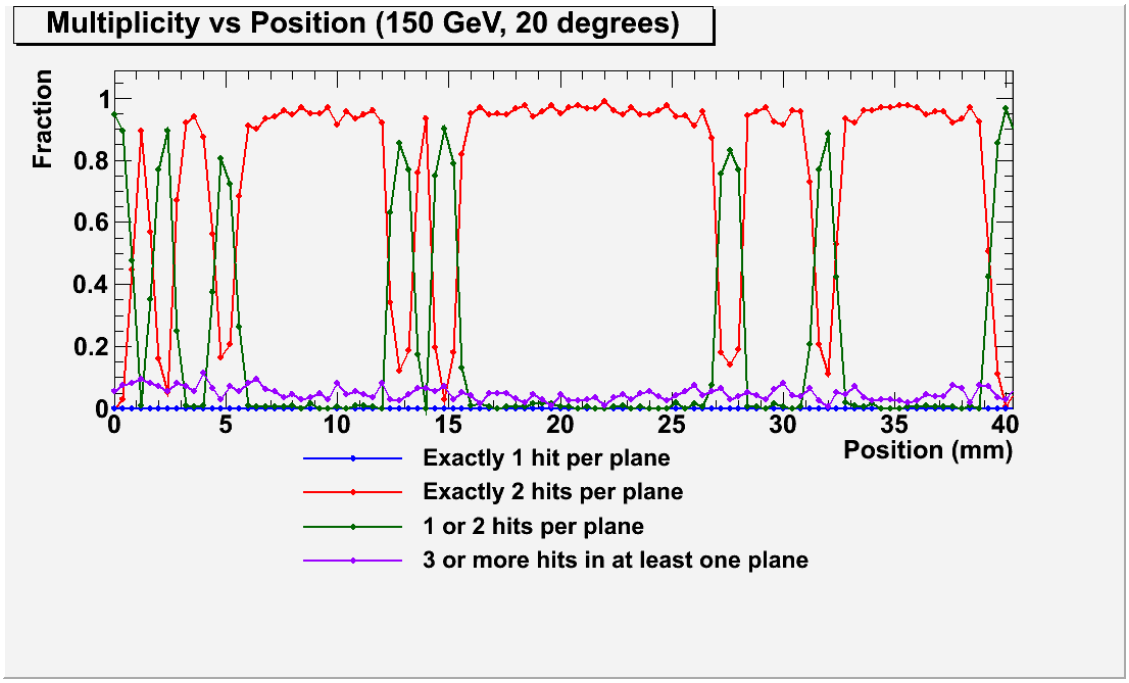

Figure 26: Multiplicity vs Position along cell for muons at $\theta, \phi = 20°$ (Linear Scale).

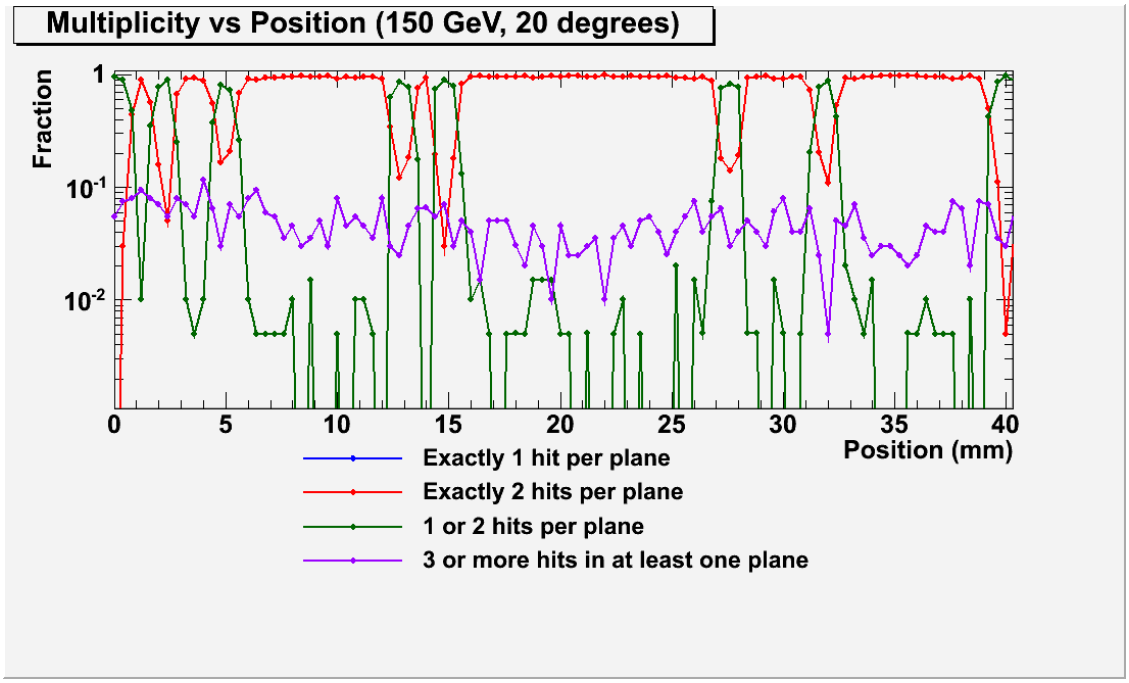

Figure 27: Multiplicity vs Position along cell for muons at $\theta, \phi = 20°$ (Log Scale).

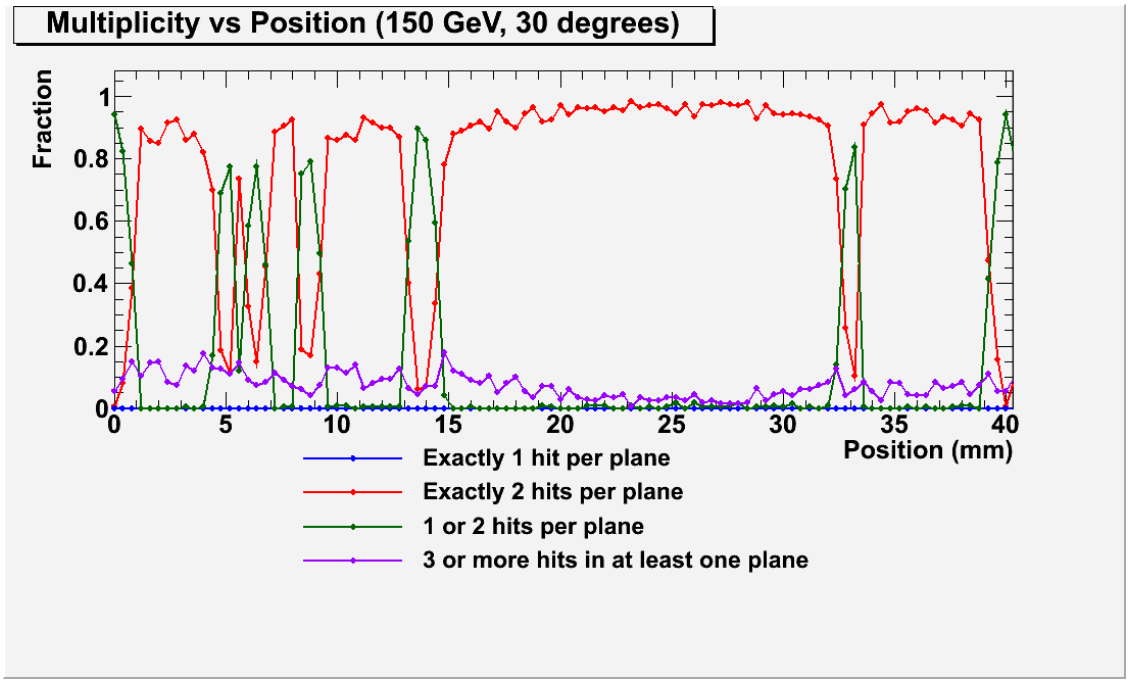

Figure 28: Multiplicity vs Position along cell for muons at $\theta, \phi = 30°$ (Linear Scale).

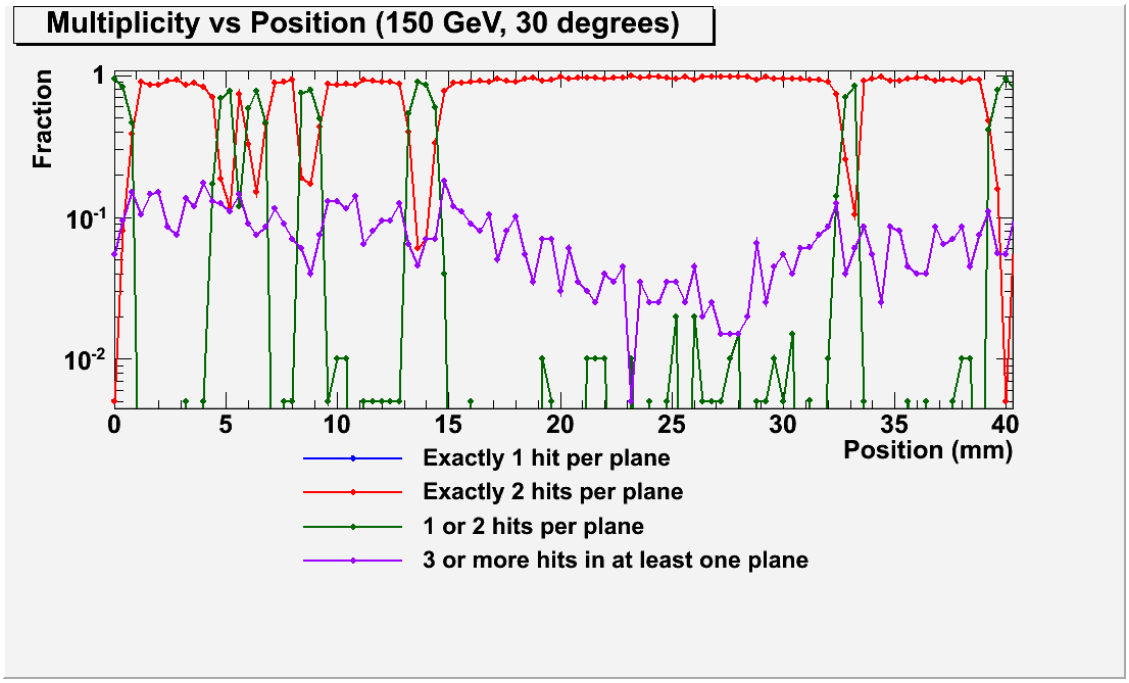

Figure 29: Multiplicity vs Position along cell for muons at $\theta, \phi = 30°$ (Log Scale).

The fraction of muons that hit 3 or more connected cells in at least one plane reaches as high as 25% in some cases. To avoid omitting them outright, which would cause a significant data loss, a refinement algorithm was developed. In each cluster of hits, the most energetic collision was chosen, and then paired with the most energetic of the adjacent collisions. The charts below investigate the success rate of this algorithm.

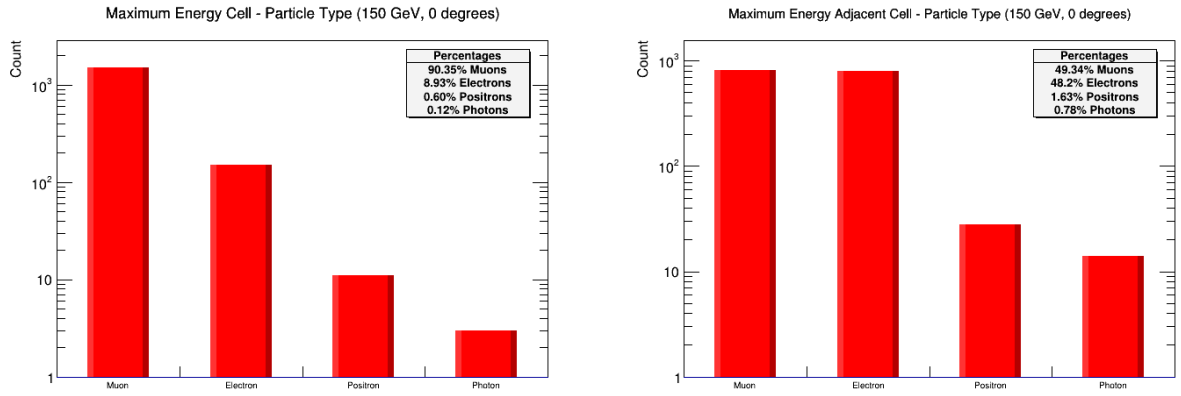

Figure 30: Maximum Energy bar charts for muons at normal incidence.

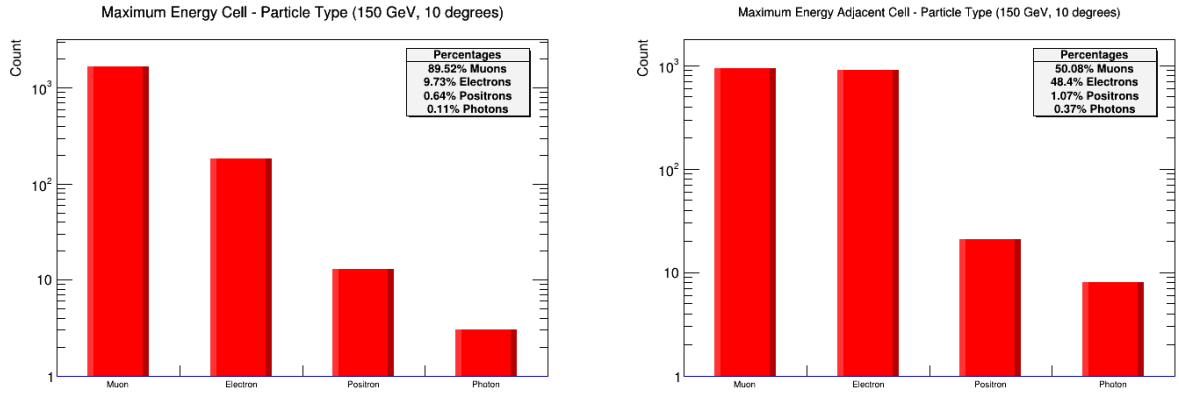

Figure 31: Maximum Energy bar charts for muons at normal incidence.

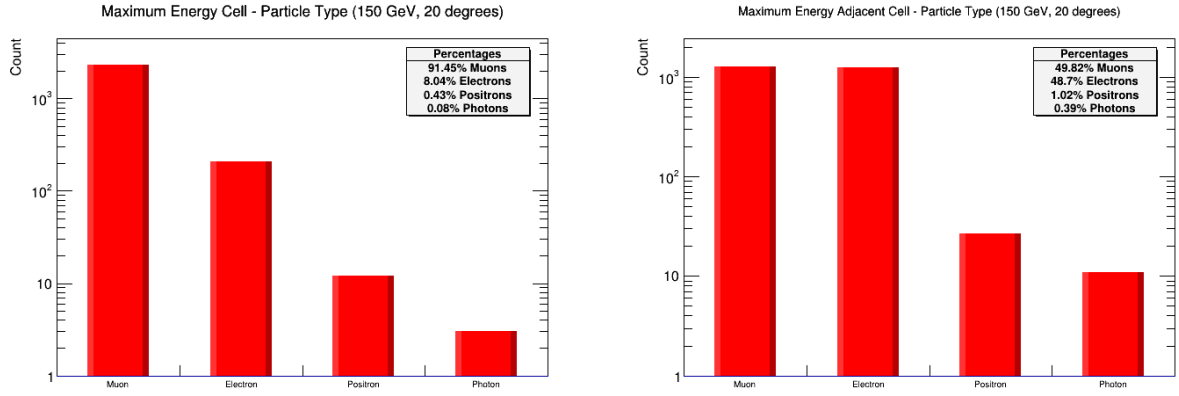

Figure 32: Maximum Energy bar charts for muons at normal incidence.

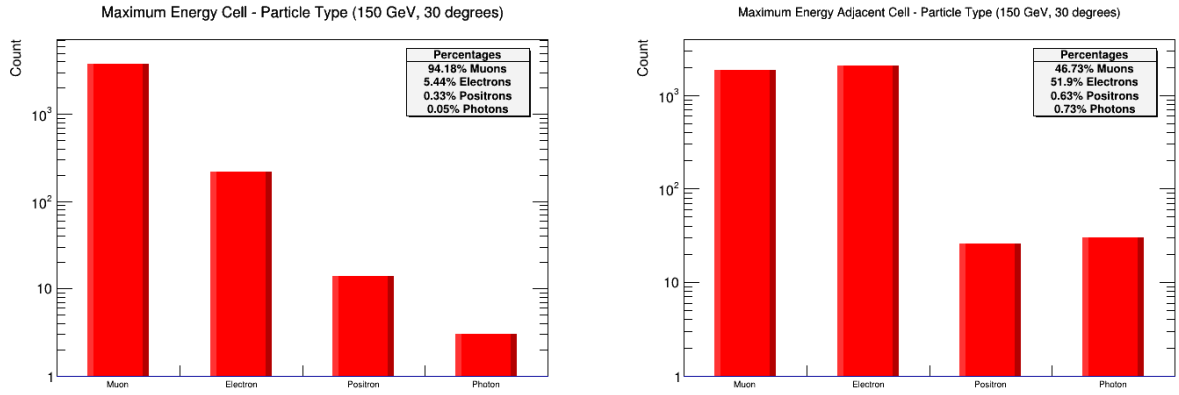

Figure 33: Maximum Energy bar charts for muons at normal incidence.

The algorithm successfully identifies both muon collisions for 45% of clusters with 3 or more hits. Thus, for particular angles and positions along the cell, up to 12% of tracks might be inaccurately reconstructed due to secondary generated by the muon. However, because these reconstructions are only erroneous when one muon track cell has significantly more deposited energy than the other, they do not cause significant error, as shown below.

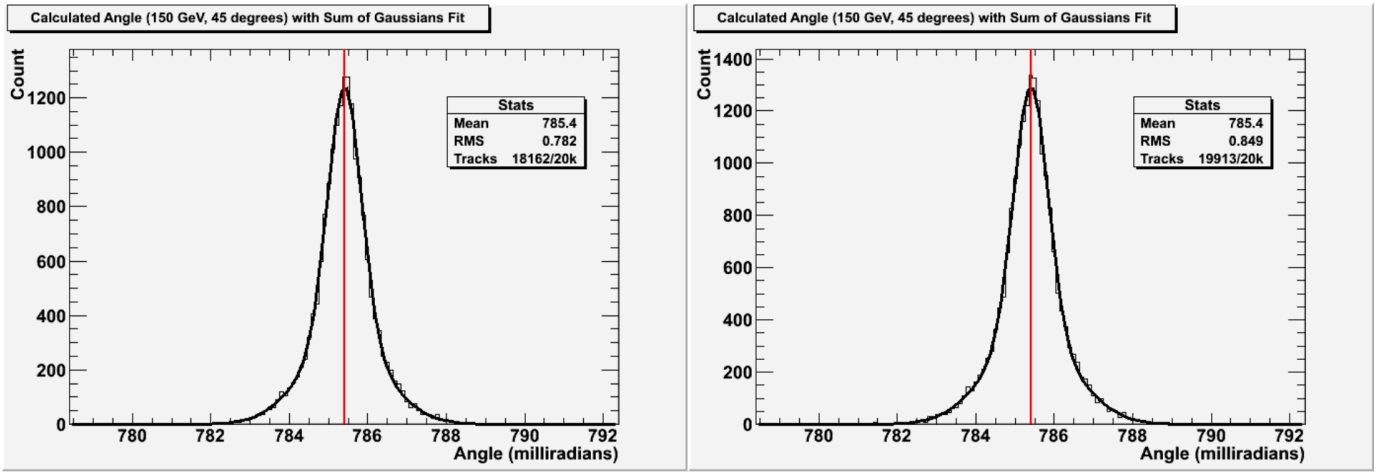

Figure 34: Comparison of angular resolution histograms with sum of gaussians fits. On the left is the resultant histogram from omitting high-multiplicity hits; on the right is the distribution obtained when using the refinement algorithm.

In this extreme case, where the greatest number of secondaries are produced, the RMS improvement is very slight; it is less than $\frac{1}{10}$ of a milliradian. This is likely a result of the algorithm for calculating RMS, as the distribution is effectively identical in both plots. However, omitting high multiplicity hits causes a 9% cut in muon track use. Thus, the refinement algorithm is the more efficient option.

6.3 Counter Response

6.3.1 Rectangular Model

As the previous discussions imply, multiplicity is heavily dependent on the geometry of a given event in both rectangular and vernier detectors. To explore this pattern in greater detail, we calculated the expected response of each counter type, in terms of energy deposition, given a variety of incident angles and hit positions. The effects of secondary particles were disregarded; only the energy deposited by the primary muon was considered.

The rectangular counter response map is shown in Figure 35. Data for this table were obtained by calculating the salient path length in two adjacent scintillator strips, then converting this quantity to MeV based on $\langle \frac{dE}{dx} \rangle$ for muons in polyvinyltoluene [4]. Green table entries indicate situations that result in only one strip with charge, while those in blue indicate situations in which both strips have some charge. As with the simulated multiplicity data in Figures 19 and 20, greater angles are more likely to yield two strips hit; this also makes sense geometrically.

Angle (Deg) \ Position (cm)	0.00	0.50	1.00	1.50
0.00	Cell 1: 4.04 Cell 2: 0.00	Cell 1: 4.04 Cell 2: 0.00	Cell 1: 4.04 Cell 2: 0.00	Cell 1: 4.04 Cell 2: 0.00
5.00	Cell 1: 4.05 Cell 2: 0.00	Cell 1: 4.05 Cell 2: 0.00	Cell 1: 4.05 Cell 2: 0.00	Cell 1: 4.05 Cell 2: 0.00
10.0	Cell 1: 4.10 Cell 2: 0.00	Cell 1: 4.10 Cell 2: 0.00	Cell 1: 4.10 Cell 2: 0.00	Cell 1: 4.10 Cell 2: 0.00
15.0	Cell 1: 4.18 Cell 2: 0.00	Cell 1: 4.18 Cell 2: 0.00	Cell 1: 4.18 Cell 2: 0.00	Cell 1: 3.90 Cell 2: 0.28
20.0	Cell 1: 4.30 Cell 2: 0.00	Cell 1: 4.30 Cell 2: 0.00	Cell 1: 4.30 Cell 2: 0.00	Cell 1: 2.95 Cell 2: 1.35
25.0	Cell 1: 4.46 Cell 2: 0.00	Cell 1: 4.46 Cell 2: 0.00	Cell 1: 4.46 Cell 2: 0.00	Cell 1: 2.39 Cell 2: 2.07
30.0	Cell 1: 4.66 Cell 2: 0.00	Cell 1: 4.66 Cell 2: 0.00	Cell 1: 4.04 Cell 2: 0.62	Cell 1: 2.02 Cell 2: 2.64
35.0	Cell 1: 4.93 Cell 2: 0.00	Cell 1: 4.93 Cell 2: 0.00	Cell 1: 3.52 Cell 2: 1.41	Cell 1: 1.76 Cell 2: 3.17
40.0	Cell 1: 5.27 Cell 2: 0.00	Cell 1: 4.71 Cell 2: 0.56	Cell 1: 3.14 Cell 2: 2.13	Cell 1: 1.57 Cell 2: 3.70
45.0	Cell 1: 5.71 Cell 2: 0.00	Cell 1: 4.28 Cell 2: 1.43	Cell 1: 2.86 Cell 2: 2.86	Cell 1: 1.43 Cell 2: 4.28

Figure 35: A map of expected energy deposition (MeV) in two adjacent rectangular scintillator strips as angle and position vary. Here, "angle" refers to the amount by which the incoming muon differs from normal incidence; "position" refers to the distance between its initial hit position and the edge of the strip. Cases that yield only one strip with charge are shown as green table entries, and those that yield two are shown in blue.

6.3.2 Vernier Model

Energy response as a function of position along the cell is plotted below.

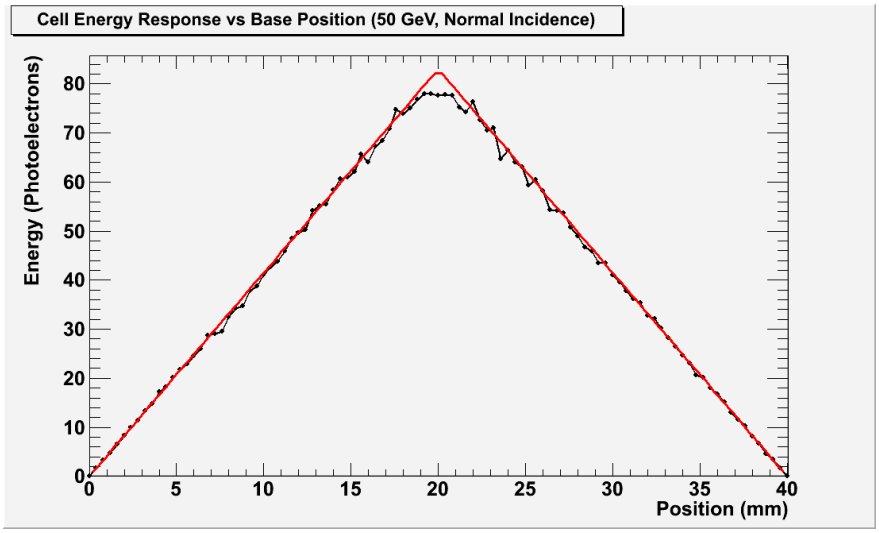

Figure 36: Energy in photoelectrons as a function of position along the cell base. 0 mm is the edge of the cell, moving up.

The response behaves as predicted, with uncertainties created by light-yield smearing. The rounded tip is likely caused by the fiber-hole and will be exacerbated by the extrusion, but does not result in significant tracking error.

7 Intrinsic Resolution: Vernier Model

7.1 Angular RMS

The angular RMS values for select energies and angles were tabulated, using the refinement algorithm. The muon track's position was scanned across the base of the cell as shown in Figure 21.

Vernier Angular RMS Table (milliradians)

Muon Energy (GeV) \ Angle (degrees)	0	5	10	15	20	25	30	35	40	45
5	1.482	1.454	1.458	1.533	1.552	1.622	1.611	1.628	1.633	1.661
10	0.993	0.967	0.989	1.026	1.037	1.055	1.044	1.035	1.009	0.960
15	0.889	0.857	0.884	0.934	0.930	0.953	0.943	0.925	0.874	0.812
20	0.860	0.815	0.867	0.895	0.915	0.921	0.914	0.892	0.829	0.764
30	0.815	0.801	0.835	0.849	0.869	0.898	0.874	0.845	0.801	0.735
40	0.805	0.808	0.829	0.850	0.867	0.893	0.877	0.837	0.784	0.723
50	0.802	0.782	0.842	0.848	0.849	0.885	0.873	0.846	0.790	0.713
75	0.800	0.791	0.839	0.843	0.846	0.881	0.881	0.825	0.767	0.700
100	0.802	0.812	0.835	0.846	0.827	0.879	0.891	0.813	0.768	0.716
150	0.808	0.795	0.830	0.851	0.862	0.881	0.878	0.817	0.777	0.721

Figure 37: Angular RMS Table for vernier detector. Energies are in GeV. Angles are measured in degrees from normal incidence. Angular RMS is in milliradians.

7.2 Positional RMS

For 50 GeV muons, the positional RMS as a function of position along the cell is plotted in Figure 38.

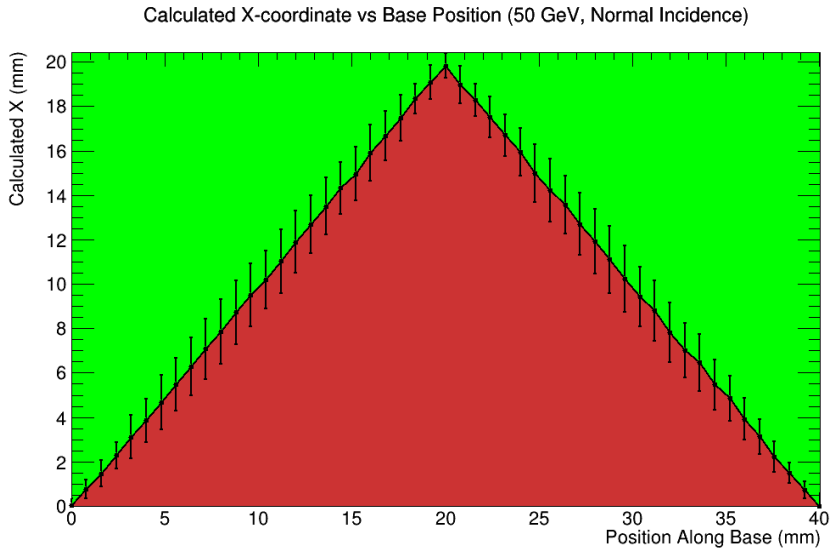

Figure 38: Plot of algorithm-calculated position vs cell base position of position-scanned triangles, with error bars. Colors added for visualization; 0 mm indicates the apex of the green triangle. The calculation is most precise at the peaks of triangles, as expected.

As predicted by the multiplicity plots in Section 6.2, the RMS is best at the peaks of either triangle.
Histograms of positional RMS for normal incidence and incident angles of 15, 30, and 45 degrees are plotted in Figure 49. These trials included a full positional scan of the cell base.

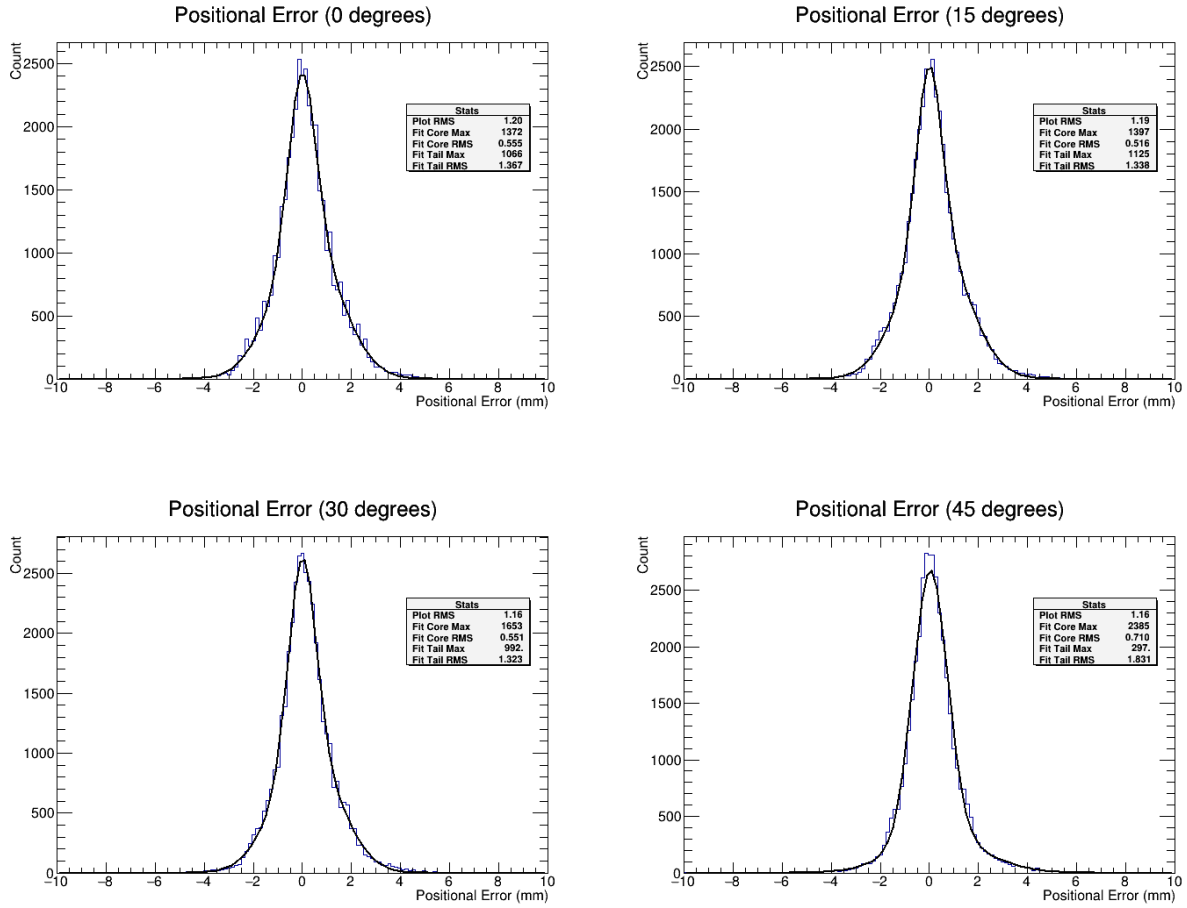

Figure 39: Histogram of positional error of muons at normal incidence and at 15°, 30°, and 45° from normal incidence.

The positional error summed over the above angles is plotted in Figure 40.

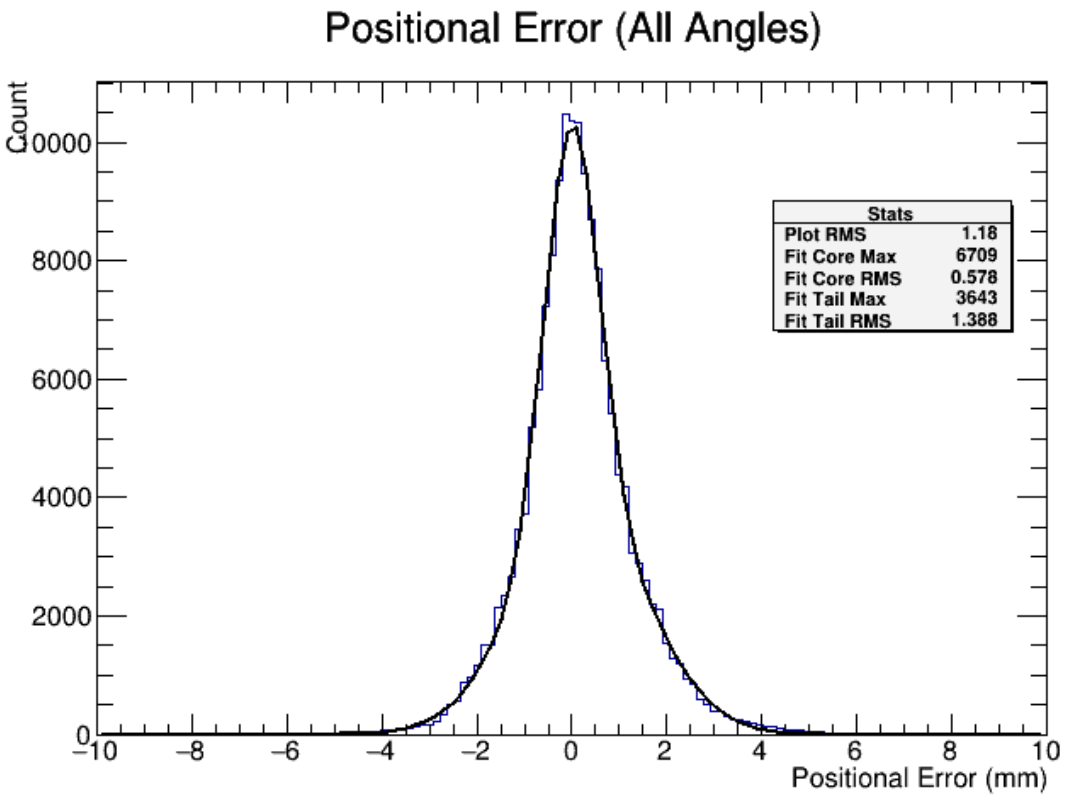

Figure 40: Histogram of positional error of muons across 15° increments.

8 Positional Back-projection Comparison with Concrete Scattering

One of the toy model's primary goals is to determine the strip size needed for optimum detector resolution. A detector with sufficient resolution should result in an uncertainty comparable to or somewhat smaller than any multiple scattering effects from the pyramid; however, a detector with too-fine resolution results in an unnecessarily high channel count and therefore unnecessary cost. So, it is of interest to calculate the particles' hit positions at the detector planes, back-project the resulting trajectory to its starting place (or any other point desired), and compare the uncertainty inherent in this process to that arising from scattering.

8.1 Rectangular Model

As discussed in section 6.1, these studies used only those events that survived the "singles cut," i.e., those that yielded exactly one hit per detector plane. We therefore took the hit position in a given plane to be the center of the strip with non-zero energy deposition. Each plane gave either a u or a v coordinate (see section 4.1), and these were combined to give one point in space for each detector.

The RMS error associated with a rectangular strip of width A is given by

$$\sigma = \frac{A}{\sqrt{12}} \tag{3}$$

so, for the 2-cm strips used here, $\sigma = \frac{0.02\,m}{\sqrt{12}}$ or c. 0.01 m. The calculated positions and their uncertainties can be back-projected to any plane by simply inserting them into the equation of a line (see Figure 41):

$$\frac{X - X_A}{X_B - X_A} = \frac{Y - Y_A}{Y_B - Y_A} = \frac{Z - Z_A}{Z_B - Z_A} \tag{4}$$

where (X_A, Y_A, Z_A) and (X_B, Y_B, Z_B) are the global coordinates corresponding to the hit positions at detectors one and two, respectively, and (X, Y, Z) are the coordinates of the back-projected point. The result is a "circle of confusion," determined by the radius r_Y in Figure 41, that represents the detector system's inherent uncertainty at the distance in question. The goal, then, is to find a strip width for which this radius does not differ substantially from the deviation caused by multiple scattering.

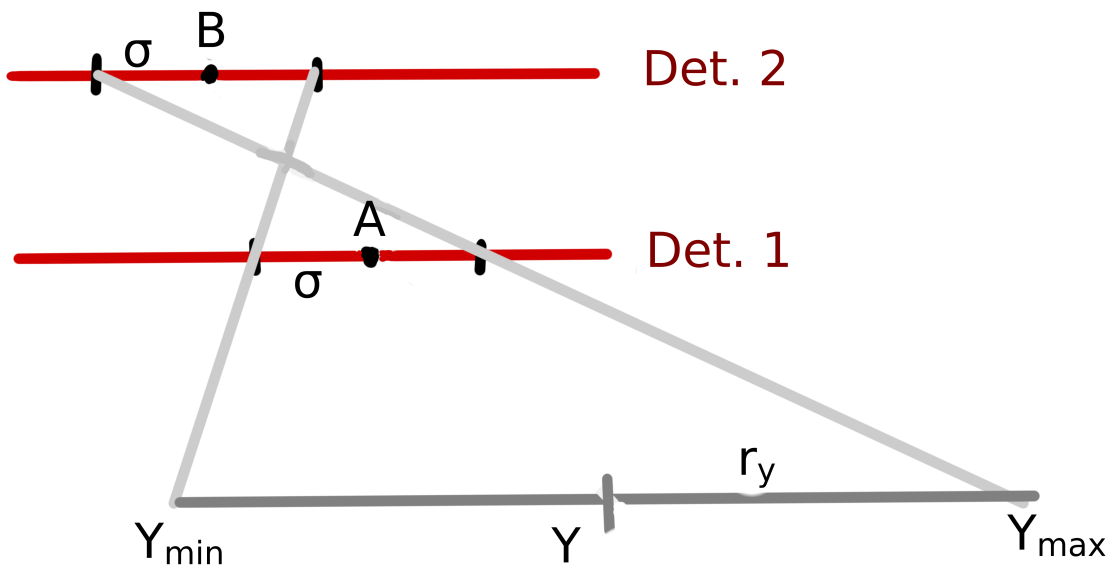

Figure 41: A 2D sketch of how the RMS "circle of confusion" radius is calculated. Since the strip width is the same in all planes, σ is the same for detectors one and two.

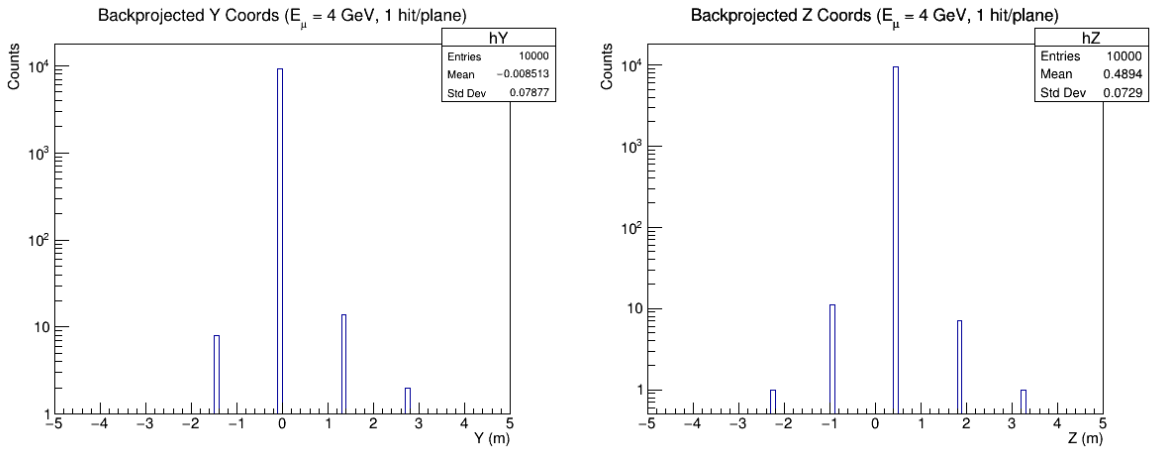

Figure 42: Preliminary results from the back-projection algorithm, using a run of 10,000 4-GeV muons and no concrete. The only events used were those that produced one hit strip per detector plane; the beam was placed at normal incidence at the center of the target strips. Trajectories were then projected a distance of 140 m, corresponding to the hypothetical center of the pyramid and the origin of the global coordinate system.

To validate the Root macro that back-projects these trajectories (**without** uncertainties), we began with a run of 10,000 4-GeV muons at normal incidence to the detectors, and this run did not include concrete. The calculated hit positions were back-projected 140 m, which corresponds to a point 0.49 m above the - here hypothetical - center of the pyramid's base (see Figs. 10, 11). Two one-dimensional histograms containing the resulting Y and Z coordinates are given in Figure 42. In both dimensions, the majority of events yielded correct starting positions (Y = -0.01 m and Z = 0.49 m respectively). Both distributions

also have a very few values in non-central bins. The discrete locations at which these values occur, combined with the fact that they vanish for higher values of E_μ, indicate that they arise from muons that scatter to strips adjacent the target. So, the algorithm successfully back-projects trajectories as desired.

8.1.1 Example Study: Void 25 m from Pyramid Surface

Here we consider an example scenario in which there is a void of interest 25 m from the pyramid's surface, and we compare the back-projection uncertainty arising from multiple scattering to the RMS error inherent in the scintillator strips.

For the purposes of this simulation, our scenario can be modeled by a 25-m long concrete block placed 25 m from the first plane of detector one. Initially, for simplicity, the particles exiting the pyramid were represented by a normal beam of 10,000 50-GeV muons placed just upstream of the concrete (see Figure 14, for example). These trajectories were then back-projected from their calculated hit positions to the far end of the concrete, a total of 50 m from detector one. Figure 43 shows the results of this projection.

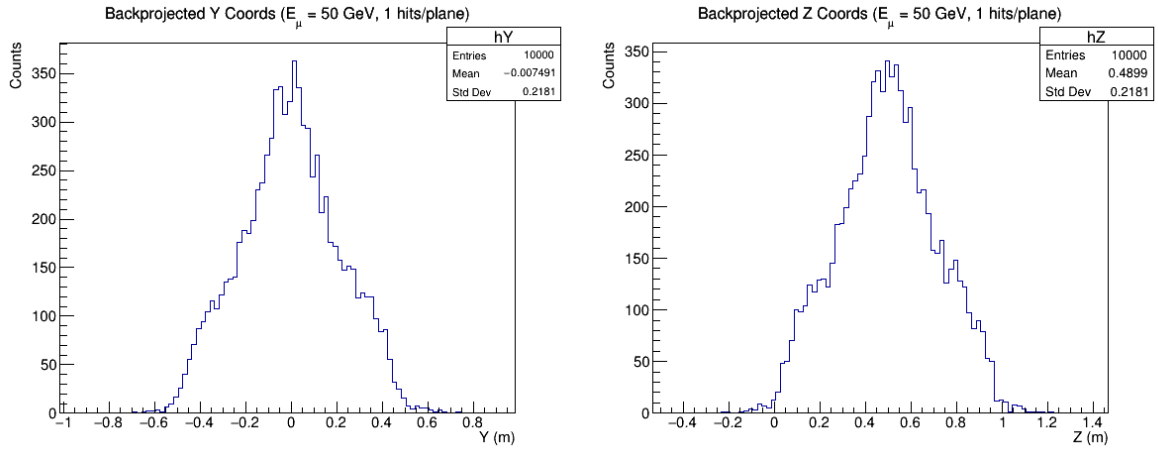

Figure 43: Results from the back-projection algorithm for a run including a 25-m block of concrete. The 10,000 50-GeV muons from this run were back-projected to the far end of the block - i.e., 50 m from detector 1 and 89 m from the hypothetical pyramid center. The resulting distribution is a reflection of multiple-scattering effects in the concrete; comparing the standard deviations of this and similar results to the RMS error of the scintillator strips provides insight on the strip size needed for sufficient position resolution.

Both plots are again centered on the beam's true starting point (as before, Y = -0.01 m and Z = 0.49 m). The continuous distributions in this case, however, directly reflect the effects of multiple scattering inside the concrete.

Using the calculation method outlined in Figure 41, the RMS circle of confusion radius coming solely from the detector resolution is approximately r = 0.29 m. This is slightly larger than, but quite similar to, the standard deviation of about 0.22 m in both plots above. In this highly specific scenario, then, a 2-cm rectangular scintillator design would likely have sufficient resolution. However, a thinner rectangle or a triangular design might still provide advantages, as we do not want the inherent detector resolution to affect our capability of detecting various unknowns in the pyramid. More work is needed to settle this question.

8.2 Vernier Model

New trials were run without positional scanning to determine positional resolution. Muons were oriented such that they were at $y = z = 1.27$m when halfway between the detectors, as shown:

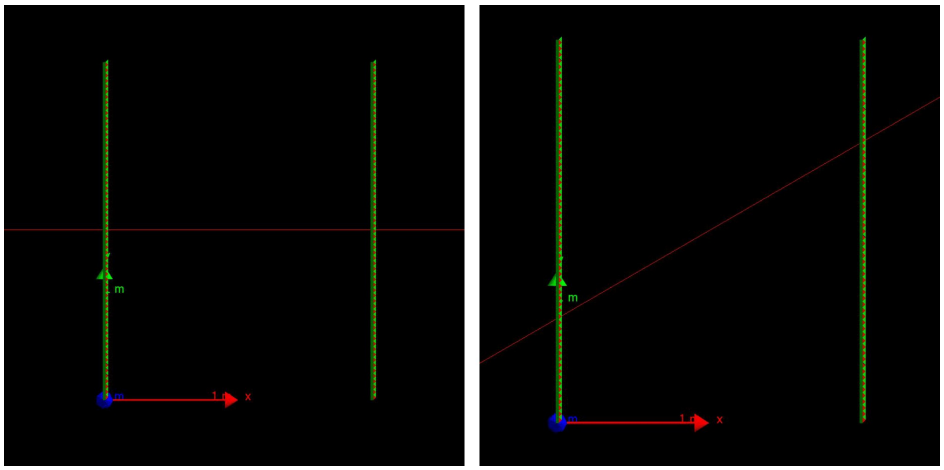

Figure 44: Plan view of muons at normal incidence and at $\theta, \phi = 30°$ passing through the point (1 m, 1.27 m, 1.27 m).

For trials with concrete, the concrete was placed and angled such that the muon traveled perpendicular to the length of the concrete, and thus path length through the concrete did not vary with angle. All secondaries generated in the concrete were killed.

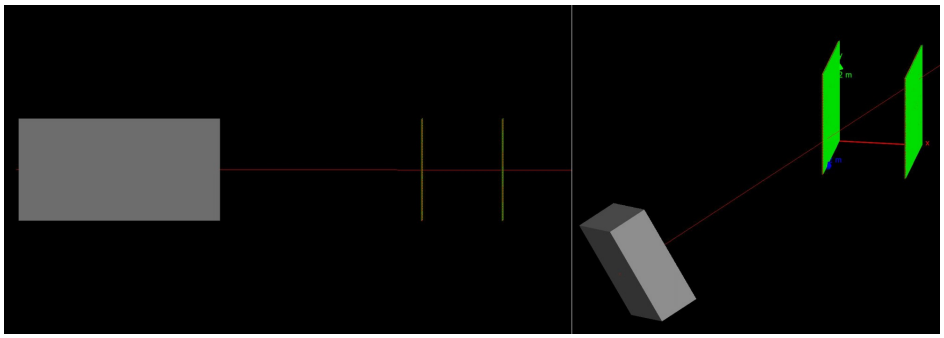

Figure 45: Visualization of concrete trials - left is 5 m concrete and muons at normal incidence, right is with 1 m concrete and muons at $\theta, \phi = 30°$.

8.2.1 Example Study: Void 25 m from Pyramid Surface

First, to compare to the example study from section 8.1.1, a 50 m back-projection (25 m from the surface of the pyramid) was done with and without a 25 m concrete block. Muons traveled normal to the concrete, and had incident energy 50 GeV (before traveling through concrete). This was compared to 50 GeV muons passing through no concrete. Below are the positional contour plots for both trials.

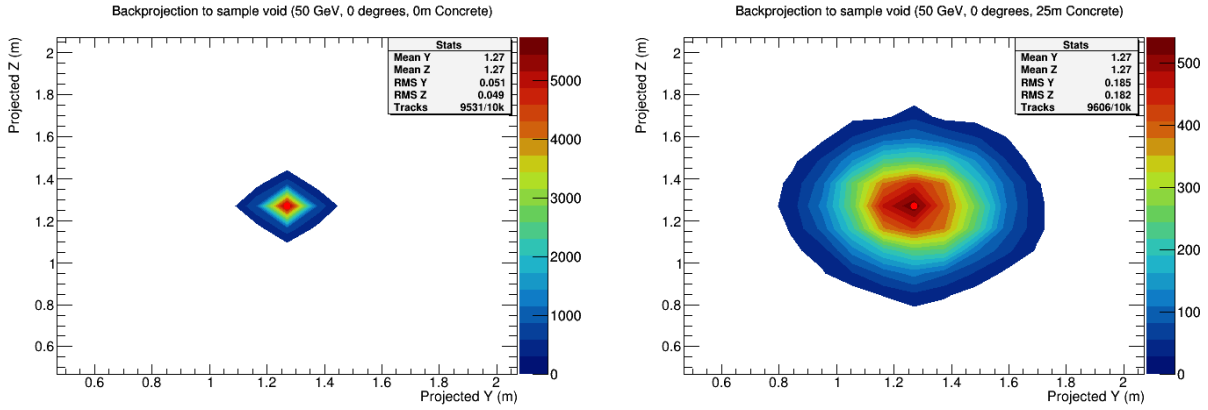

Figure 46: Comparison of 50 m positional projections of 50 GeV muons at normal incidence passing through 0 m concrete and 25 m concrete.

The positional RMS without concrete is significantly smaller than that with concrete, so the inherent uncertainty in the detector is negligible in this scenario. Thus, the vernier detector performs better than the rectangular cell detector and is sufficient for this example. Further trials with concrete are discussed in Appendix A.2.

8.2.2 Back-projections to Significant Features

Here, we consider the path of a muon that reaches our detectors from a given notable feature within the pyramid. We first found the expected RMS multiple scattering of the particle analytically; then, we compared this value with the results of a simulation which studied scattering based on a concrete pyramid dummy and back-projected the inherent detector uncertainty to the relevant location in the pyramid.

Table 3 shows the calculated approximate distance from various chambers of interest to the closest detector, as well as the length of the path in the pyramid that a muon travels to reach the center of that detector from the feature in question. The resulting multiple scattering for muons of 50 and 150 GeV is also given. To calculate all distances and path lengths, we assumed that there was one cargo container centered on each side of the pyramid, as in Figure 11, and that each detector was 3 m. in height. To convert the pyramid path length from m. to radiation lengths, we assumed that the pyramid was composed of solid concrete, which has a characteristic radiation length of 0.1155 m [4].

From this table and the following equation for RMS of multiple-scattering of muons (used in the final two columns):

$$\sigma_\theta = \frac{0.0136}{E}\sqrt{\frac{x}{X_0}}\left[1 + 0.038\ln\left(\frac{x}{X_0}\right)\right] \tag{5}$$

where σ_θ is in radians, E is muon energy in GeV, x is path length, and X_0 is radiation length (0.1155 m for concrete - see above), we deduce that the angular scattering of muons from these features eclipses the RMS error in the detector. Simulated back-projection comparisons with and without concrete to these locations is shown in Figures 47 through 50. Muon energies ranged from 5-150 GeV upon hitting the detector.

Feature	(X_f, Y_f, Z_f)	Closest Detector	Distance to Detector (m)	Path Length in Pyramid (m)	PL in Pyramid (rad. lengths)	RMS Multiple Scattering - 50 GeV (milliradians)	RMS Multiple Scattering - 150 GeV (mr)
King's Chamber	(2.44, -15.0, 49.9)	South	134	94.0	814	9.74	3.24
Queen's Chamber	(4.80, -3.88, 27.9)	East	138	106	918	10.4	3.46
Grand Gallery	(7.15, 16.0, 40.9)	North	130	93.9	813	9.74	3.24
Phantom Chamber	(0, -10.0, 120.)	South	183	30.6	265	5.37	1.79

Table 3: Calculated path length and multiple scattering in the pyramid for a muon coming from various features of interest. For the three final columns, we used concrete as a stand-in for the material of the pyramid.

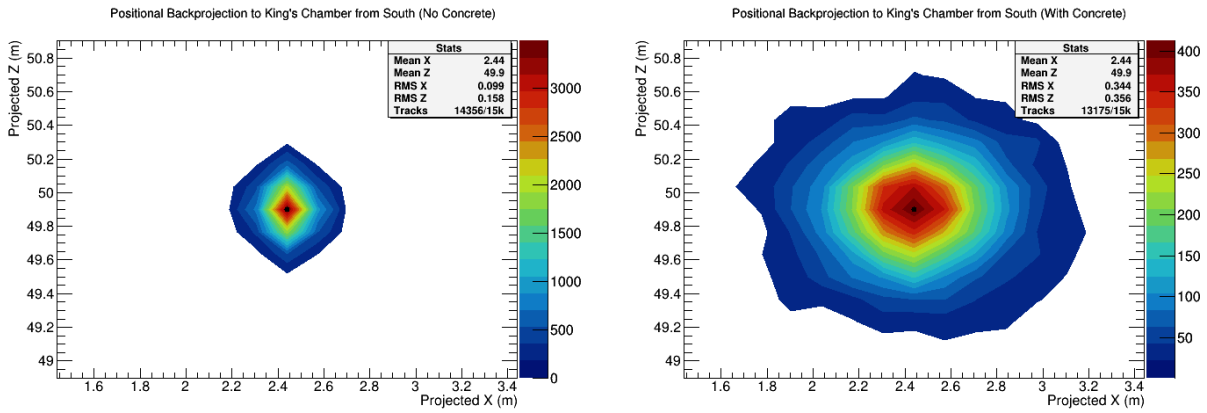

Figure 47: Positional back-projection to King's Chamber from South, with and without concrete.

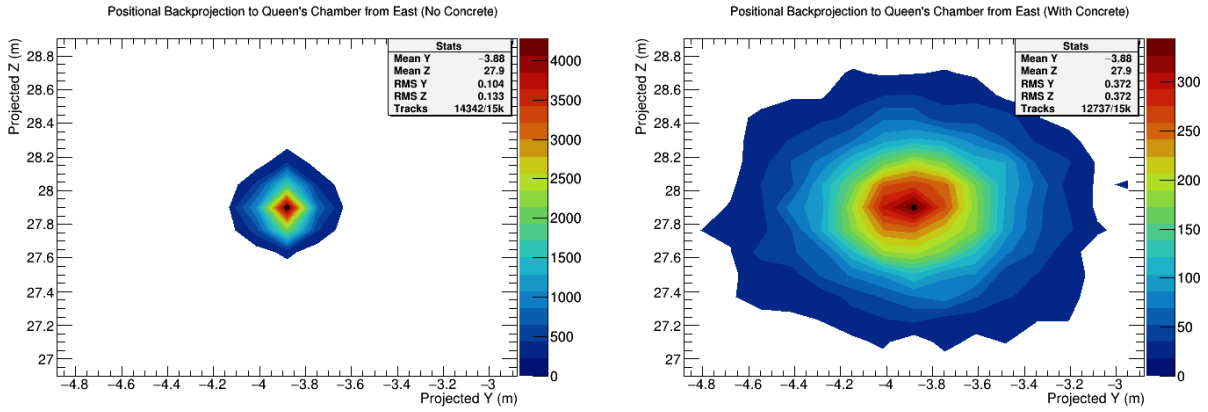

Figure 48: Positional back-projection to Queen's Chamber from East, with and without concrete.

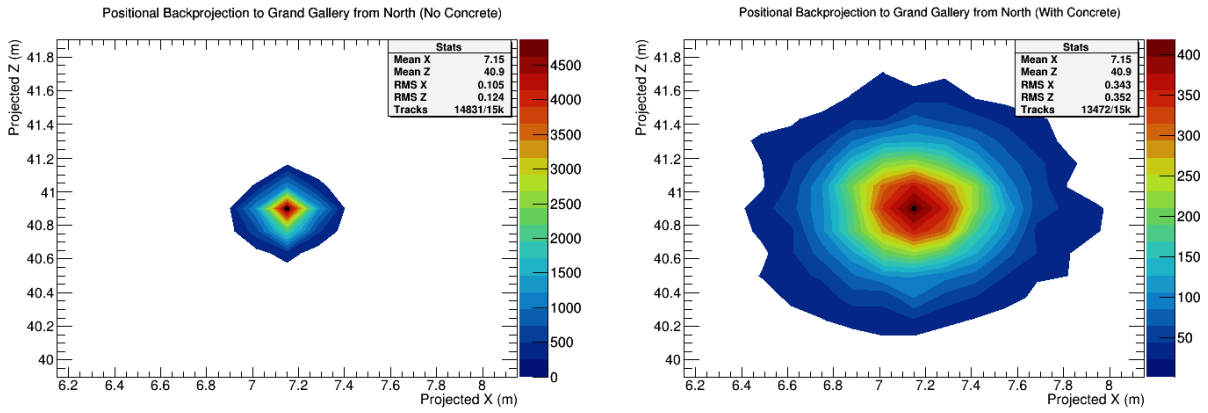

Figure 49: Positional back-projection to Grand Gallery from North, with and without concrete.

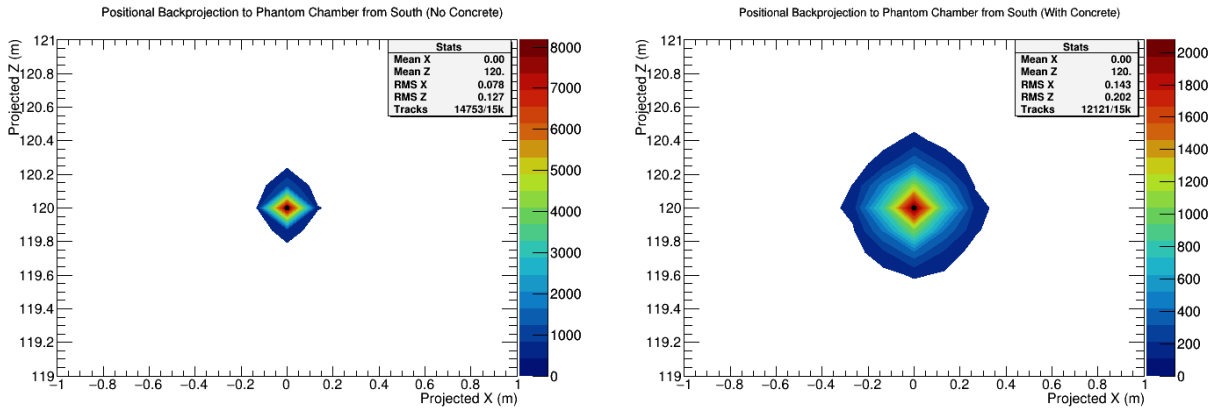

Figure 50: Positional back-projection to Phantom Chamber from South, with and without concrete.

9 Toy Model: Summary

9.1 Discussion

While multiplicity is only a source of error for the rectangular detector, the vernier model turns it into an advantage, allowing a more accurate reconstruction of tracks. The vernier refinement algorithm also ensures that multiplicity is not as significant a cause of uncertainty as in the rectangular case. This fundamental difference in algorithm allows the vernier detector to far outperform the rectangular, as exemplified by the example study with a simulated void in Section 8. For significant features that are known to exist within the pyramids, the resolution of the vernier detector is greatly outweighed by the uncertainty introduced by the effects of multiple scattering. This is true in most possible cases. The RMS of muons scattering in material can be approximated analytically by Equation 5. The results of this equation for select energies and lengths of concrete are tabulated below.

Scattering in Concrete

Muon Energy (GeV) \ Concrete Length (m)	1	3	5	10	15	20	35	50	75	100
5	5.542	9.981	13.11	18.98	23.56	27.47	37.00	44.73	55.49	64.66
10	2.771	4.990	6.557	9.493	11.78	13.73	18.50	22.36	27.74	32.33
15	1.847	3.327	4.371	6.329	7.856	9.157	12.33	14.91	18.49	21.55
20	1.385	2.495	3.278	4.746	5.892	6.868	9.252	11.18	13.87	16.16
30	0.923	1.663	2.185	3.164	3.928	4.578	6.168	7.456	9.249	10.77
40	0.692	1.247	1.639	2.373	2.946	3.434	4.626	5.592	6.937	8.082
50	0.554	0.998	1.311	1.898	2.356	2.747	3.700	4.473	5.549	6.466
75	0.369	0.665	0.874	1.265	1.571	1.831	2.467	2.982	3.699	4.310
100	0.277	0.499	0.655	0.949	1.178	1.373	1.850	2.236	2.774	3.233
150	0.184	0.332	0.437	0.632	0.785	0.915	1.233	1.491	1.849	2.155

Figure 51: Tabulation of expected scattering RMS according to Eq. **??** for select energies and lengths of concrete. RMS is in milliradians.

The bottom-left corner of the table generally contains cases where the effects of scattering and the vernier uncertainty are comparable. However, the angular uncertainty (as shown in Figure 37) is still on the order of a milliradian, ensuring that for a 125 m back-projection (near the center of the pyramid), the vernier would still accurately track muons to within 13 cm, allowing it to see any voids large enough to be of interest.

The cost estimate for the scintillator cells is a total of approximately $580k (not including wavelength shifting fibers). There is virtually no difference in cost between using triangular or rectangular extrusions.

9.2 Conclusions

The vernier model detector is the superior detector design. For the same cost per unit area, it provides an improvement in back-projection resolution by more than a factor of 4. Its uncertainty is dominated by the effects of multiple scattering in most cases; nonetheless, it can accurately track muons to within 13 cm of their actual position.

10 Acknowledgments

The authors thank Alan Bross and Henry Frisch for their guidance and mentorship on all aspects of the project and Ralf Ehrlich for his expert advice regarding GEANT4. We thank Anna Pla-Dalmau, Edmond C Dukes, Adam Para, Patrick La Riviere, Christian Sodano, and Leah Welty-Rieger for their feedback and guidance. S. Dukes, O. Shohoud, and T. Welch gratefully acknowledge the Physical Sciences Division, the Enrico Fermi Institute, and the College of the University of Chicago, as well as the Department of Physics at the University of Virginia and Virginia Tech.

References

[1] L. Alvarez, A. Jared, F. Anderson, F. Bedwei et al., *Search for Hidden Chambers in the Pyramids*, Science **167** (1970) 832-839.

[2] K. Morishima et al., *Discovery of a big void in Khufu's Pyramid by observation of cosmic-ray muons*, Nature **552** (2017) 386-390.

[3] L. Aliaga et al., *Design, calibration, and performance of the MINERvA detector*, Nuclear Instruments and Methods in Physics Research A **743** (2014) 130-159.

[4] C. Patrignani et al (Particle Data Group). Chinese Physics C, 2016 **40(10)** (2016) 100001.

[5] GEANT4 Collaboration, V. Ivanchenko, *Geant4 toolkit for simulation of HEP experiments*, Nuclear Instruments and Methods in Physics Research A **502** (2003) 666-668.

[6] "GEANT4 Tool Kit." http://geant4.cern.ch/.

[7] "G4beamline." http://www.muonsinternal.com/muons3/G4beamline.

[8] "ROOT." https://root.cern.ch/.

[9] Rene Brun and Fons Rademakers, ROOT - An Object Oriented Data Analysis Framework, Proceedings AIHENP'96 Workshop, Lausanne, Sep. 1996, Nucl. Inst. Meth. in Phys. Res. A **389** (1997) 81-86.

[10] H. D. Bui, *Imaging the Cheops Pyramid.* Springer, 2012.

A Appendix A

A.1 Variations between θ and ϕ

The Angular RMS table in 7.2 only varies and measures ϕ. Variations in θ and ϕ simultaneously cause increased uncertainty due to greater path length in the detector. New trials were run where both angles were incremented, and the RMS for each are tabulated below. Both ϕ and θ are measured in degrees from normal incidence (θ is 90° from its definition in coordinate system, for simplicity).

Muon Energy (GeV) \ θ (degrees)	0	5	10	15	20	25	30	35	40	45
5	1.319	1.331	1.401	1.446	1.416	1.529	1.554	1.710	1.855	2.134
10	0.832	0.862	0.907	0.944	0.882	0.947	0.920	1.019	1.047	1.193
15	0.734	0.775	0.811	0.850	0.767	0.846	0.793	0.875	0.889	0.995
20	0.694	0.741	0.768	0.806	0.729	0.802	0.753	0.820	0.845	0.918
30	0.668	0.711	0.748	0.783	0.705	0.774	0.723	0.788	0.790	0.886
40	0.655	0.698	0.735	0.776	0.705	0.760	0.708	0.772	0.789	0.873
50	0.656	0.701	0.742	0.774	0.698	0.755	0.705	0.771	0.778	0.869
75	0.657	0.705	0.737	0.784	0.694	0.753	0.702	0.770	0.771	0.854
100	0.658	0.689	0.746	0.781	0.694	0.754	0.706	0.761	0.767	0.854
150	0.660	0.701	0.749	0.789	0.707	0.755	0.699	0.771	0.773	0.855

Figure 52: RMS Table for θ.

Muon Energy (GeV) \ ϕ (degrees)	0	5	10	15	20	25	30	35	40	45
5	1.593	1.580	1.578	1.689	1.795	1.959	2.046	2.336	2.760	3.329
10	1.091	1.091	1.070	1.136	1.176	1.253	1.201	1.299	1.375	1.493
15	0.990	0.984	0.976	1.038	1.048	1.116	1.024	1.084	1.103	1.113
20	0.944	0.951	0.943	0.994	1.014	1.060	0.976	1.008	1.004	0.981
30	0.920	0.930	0.909	0.971	0.984	1.019	0.923	0.948	0.939	0.881
40	0.908	0.920	0.906	0.959	0.965	1.019	0.906	0.935	0.906	0.857
50	0.906	0.911	0.891	0.949	0.959	1.009	0.902	0.920	0.898	0.832
75	0.911	0.919	0.898	0.960	0.959	1.010	0.890	0.920	0.888	0.814
100	0.913	0.921	0.897	0.953	0.952	1.011	0.889	0.908	0.870	0.822
150	0.912	0.913	0.902	0.948	0.946	1.010	0.899	0.914	0.875	0.810

Figure 53: RMS Table for ϕ.

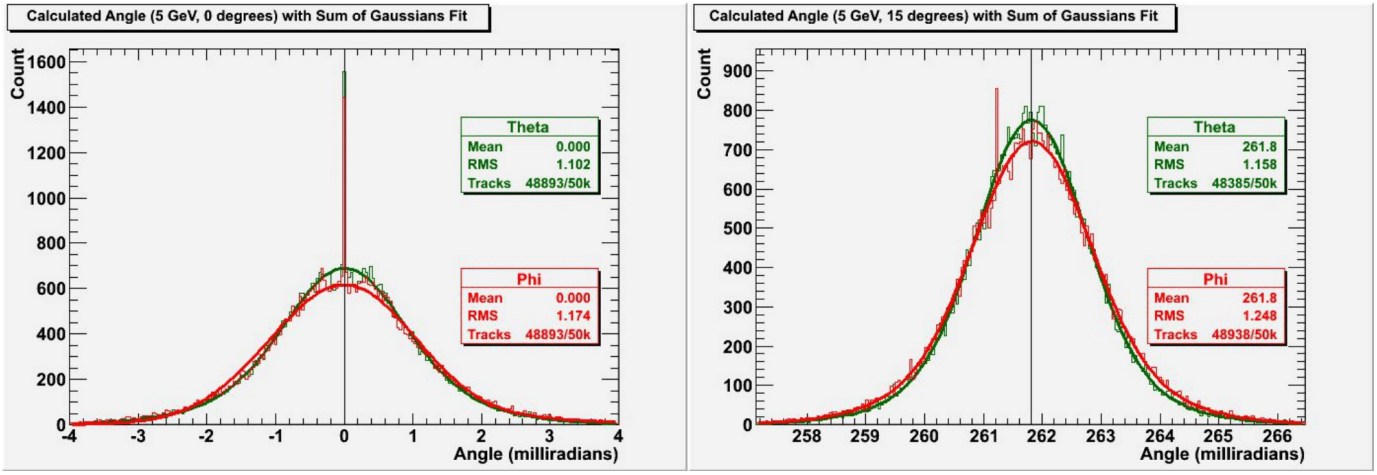

Figure 54: Calculated angle histogram for 5 GeV muons at normal incidence and at $\theta, \phi = 15°$.

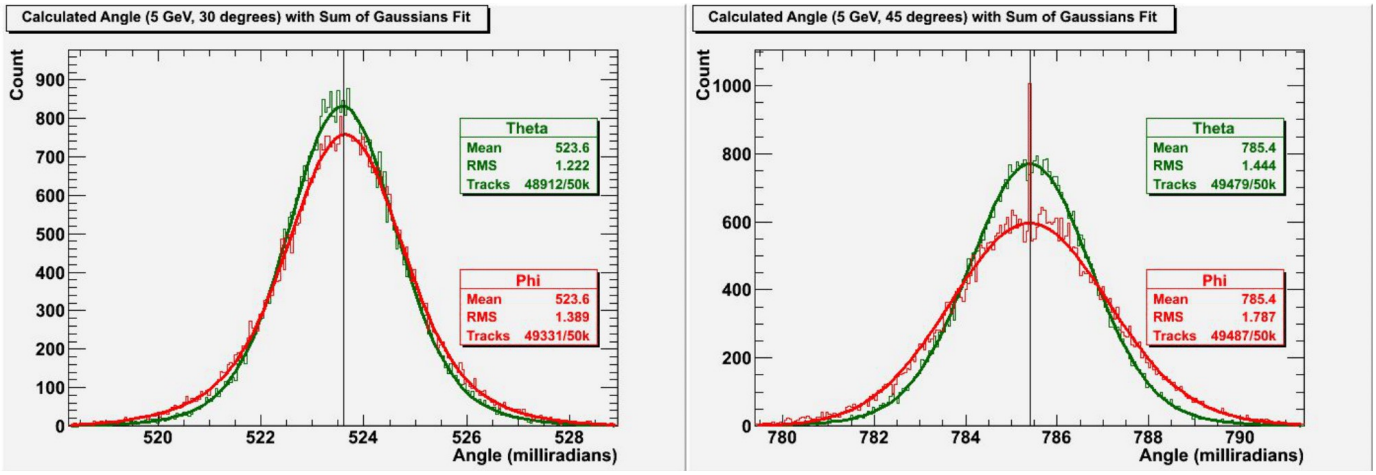

Figure 55: Calculated angle histogram for 5 GeV muons at $\theta, \phi = 30°$ and at $\theta, \phi = 45°$.

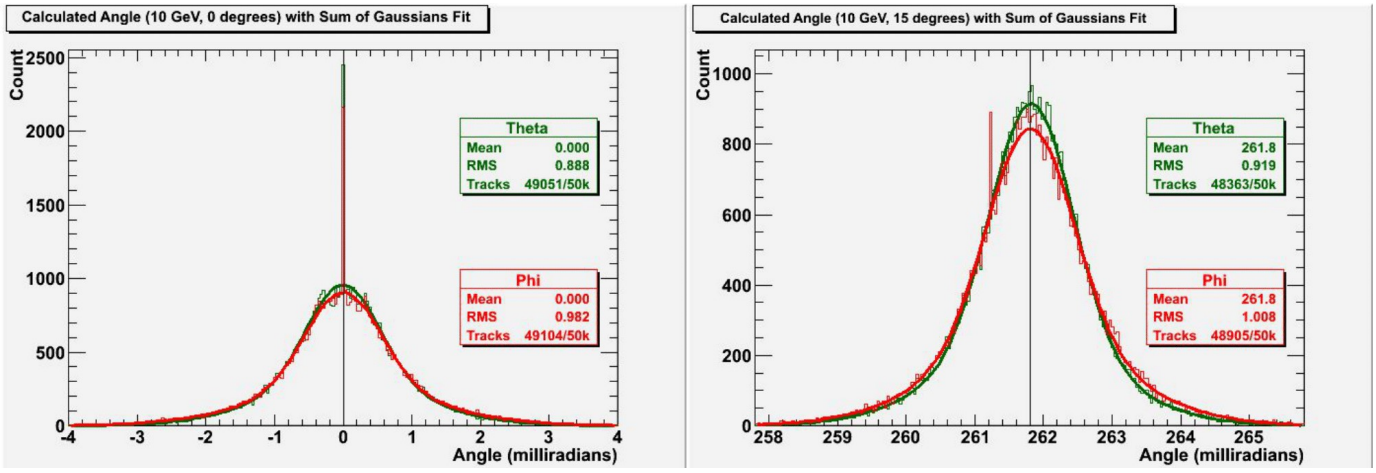

Figure 56: Calculated angle histogram for 10 GeV muons at normal incidence and at $\theta, \phi = 15°$.

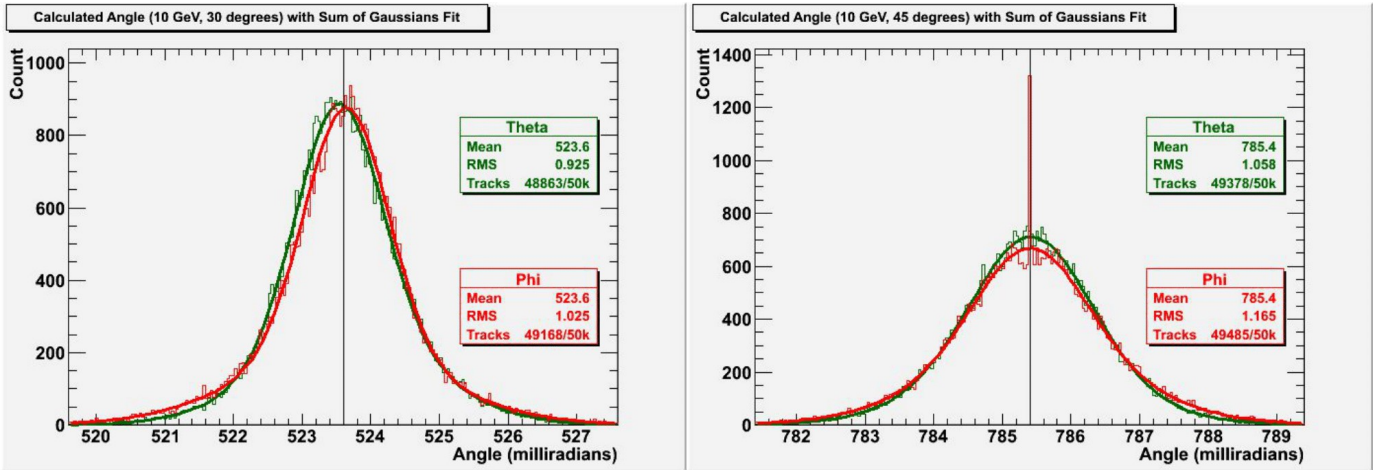

Figure 57: Calculated angle histogram for 10 GeV muons at $\theta, \phi = 30°$ and at $\theta, \phi = 45°$.

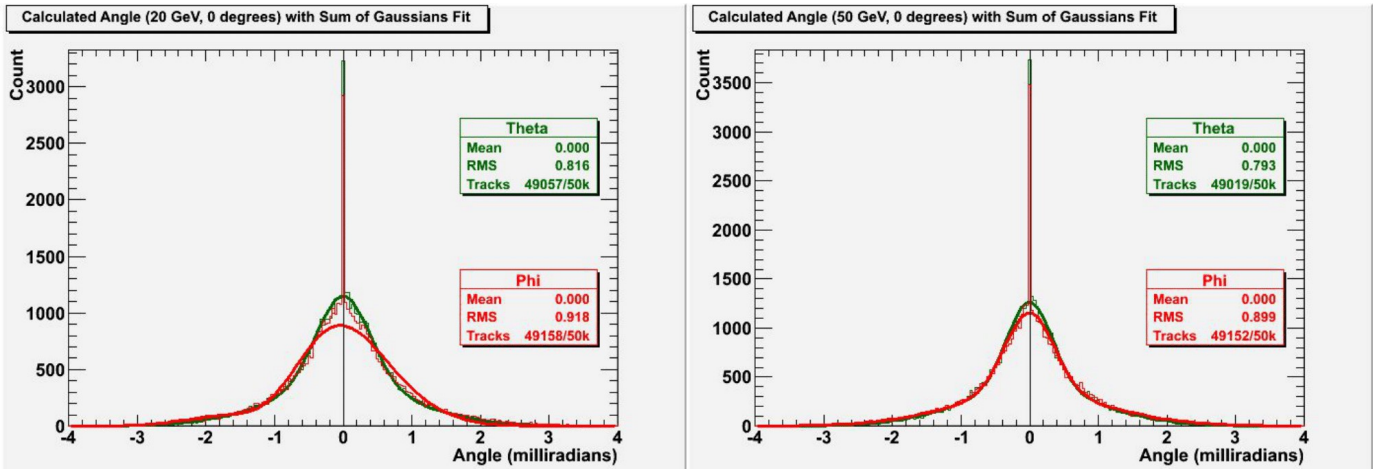

Figure 58: Calculated angle histogram for 20 GeV and 50 GeV muons at normal incidence.

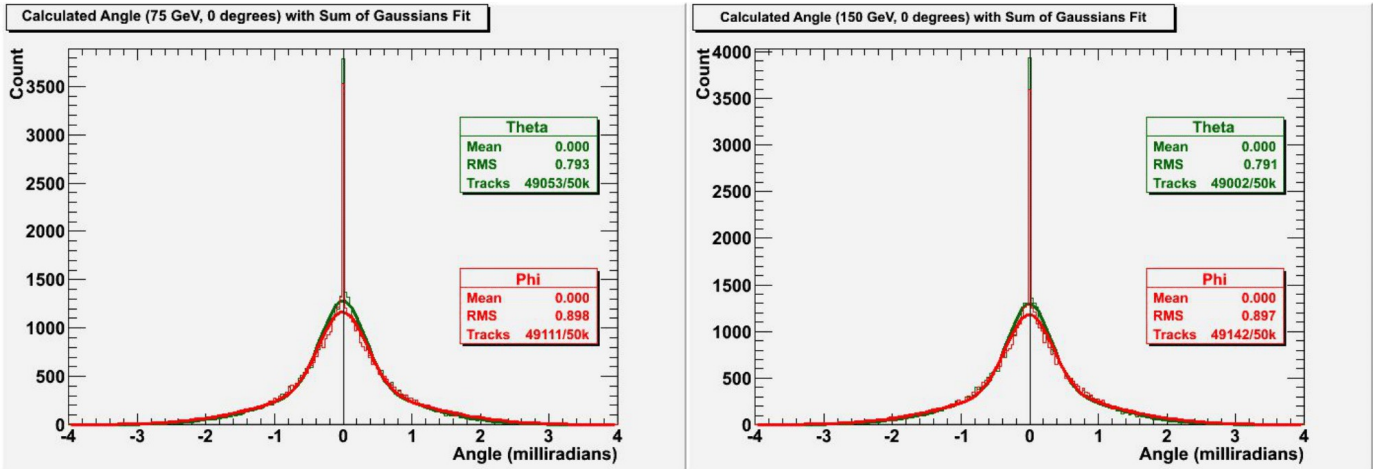

Figure 59: Calculated angle histogram for 100 GeV and 150 GeV muons at normal incidence.

For muons at normal incidence, the strong peaks at the mean are due to extremely high precision for muons that pass through a single cell in all 4 planes (see Section 6.2 on multiplicity). This removes the uncertainty introduced by the poisson distribution of $\frac{dE}{dx}$, the light-yield smearing, the fiber-hole, and histogram binning.
Causes of uncertainty are discussed in the next section.

A.2 Causes of Uncertainty

This section will investigate trends in angular RMS of the vernier detector, and identify their causes.

The uncertainty in ϕ is generally greater than in θ, which is antithetical to what the symmetry of the simulation would suggest. The only difference is the ordering of the planes; the planes in each bank that calculated θ are in front of those that calculate ϕ. Below is a comparison of RMS when the plane order is switched.

	Original		ϕ in Front	
Muon Energy (GeV)	ϕ	θ	ϕ	θ
5	1.593	1.319	1.298	1.563
10	1.091	0.832	0.826	1.097
15	0.990	0.734	0.731	0.979
20	0.944	0.694	0.691	0.948
30	0.920	0.668	0.670	0.927
40	0.908	0.655	0.662	0.917
50	0.906	0.656	0.666	0.913
75	0.911	0.657	0.660	0.926
100	0.913	0.658	0.659	0.931
150	0.912	0.660	0.661	0.930

Normal Incidence

Figure 60: Comparison of original RMS values with resultant RMS values from putting ϕ planes in front.

The RMS values have effectively swapped. Conclusively, the angular RMS of the second planes in each bank is greater than that of the first. We will investigate possible causes, namely creation of secondaries and multiple scattering.

A.2.1 Creation of Secondaries

Because the refinement algorithm is imperfect, generation of secondaries is likely a significant cause of error. This error would be more pronounced in the ϕ planes, as

secondaries would be generated while the muon passed through the θ planes. Below are RMS comparisons for when secondaries are removed.

Muon Energy (GeV)	Original		No Secondaries	
	ϕ	θ	ϕ	θ
5	1.593	1.319	0.796	0.790
10	1.091	0.832	0.340	0.342
15	0.990	0.734	0.252	0.250
20	0.944	0.694	0.216	0.215
30	0.920	0.668	0.190	0.189
40	0.908	0.655	0.181	0.181
50	0.906	0.656	0.176	0.176
75	0.911	0.657	0.172	0.172
100	0.913	0.658	0.170	0.170
150	0.912	0.660	0.169	0.169

Normal Incidence

Figure 61: Comparison of original RMS values for muons at normal incidence with resultant RMS values from eliminating secondaries.

		ϕ,θ (degrees)								
		0	5	10	15	20	25	30	35	40	45
Original	ϕ	1.593	1.580	1.578	1.689	1.795	1.959	2.046	2.336	2.760	3.329
	θ	1.319	1.331	1.401	1.446	1.416	1.529	1.554	1.710	1.855	2.134
No Secondaries	ϕ	0.796	0.845	0.854	0.923	0.999	1.128	1.296	1.558	1.982	2.604
	θ	0.790	0.825	0.853	0.881	0.899	0.958	1.019	1.113	1.245	1.507

5 GeV

Figure 62: Comparison of original RMS values for 5 GeV muons with resultant RMS values from eliminating secondaries.

The disparity between ϕ and θ disappears for high-energy muons. It is increasingly pronounced with angle for low-energy muons, however. This is likely due to scattering.

A.2.2 Multiple Coulomb Scattering

As discussed in 9.1, muons scatter as they pass through material according to Equation 5. Multiple scattering increases with path length, and therefore with angle (greater angles have greater path length through the detectors) and decreases with energy. Scattering is also more pronounced in the ϕ detectors, as the muons have already scattered in the θ detectors when they reach the ϕ detectors.

Below are the resultant RMS values values when secondaries, scattering, and the Poisson distribution of $\frac{dE}{dx}$ are removed (as a byproduct of the limitations of the simulation). The only sources of error below are the fiber-hole, light yield smearing, and multiplicity for higher values of θ (due to the construction of the coordinate system, ΔZ is dependent on both ϕ and θ. When θ and ϕ are both at higher angles, muons travel steeply enough to intersect more than 2 vernier cells in the θ planes).

	Original		No Stochastics	
Muon Energy (GeV)	ϕ	θ	ϕ	θ
5	1.593	1.319	1.08e-4	1.10e-4
10	1.091	0.832	1.6e-4	1.65e-4
15	0.990	0.734	1.05e-4	1.06e-4
20	0.944	0.694	1.05e-4	1.06e-4
30	0.920	0.668	1.05e-4	1.06e-4
40	0.908	0.655	1.05e-4	1.06e-4
50	0.906	0.656	1.05e-4	1.06e-4
75	0.911	0.657	1.05e-4	1.06e-4
100	0.913	0.658	1.05e-4	1.06e-4
150	0.912	0.660	1.06e-4	1.08e-4

Normal Incidence

Figure 63: Comparison of original RMS values for muons at normal incidence with resultant RMS values values from stochastic processes.

		ϕ,θ (degrees)									
		0	5	10	15	20	25	30	35	40	45
Original	ϕ	1.593	1.580	1.578	1.689	1.795	1.959	2.046	2.336	2.760	3.329
	θ	1.319	1.331	1.401	1.446	1.416	1.529	1.554	1.710	1.855	2.134
No Stochastics	ϕ	1.08e-4	1.16e-3	1.11e-3	9.85e-4	1.66e-3	5.69e-4	6.12e-4	8.51e-4	4.46e-4	1.08e-4
	θ	1.10e-4	1.26e-3	1.54e-3	1.27e-3	8.54e-4	9.00e-4	5.31e-4	5.50e-4	3.69e-3	9.36e-2

5 GeV

Figure 64: Comparison of original RMS values for 5 GeV muons with resultant RMS values from eliminating stochastic processes.

The RMS is on the order of a microradian, so the detectors are near perfect. Multiple scattering and secondary generation were thus the primary causes of uncertainty.

B Appendix B

B.1 Use of $\frac{dE}{dx}$ in Determining Muon Momentum

It is possible that the charge collected by the detector cells can be used to sort muons by their incident momenta. If successful, this approach could yield clearer image reconstruction by allowing us to use only those muons in an ideal energy range - eliminating too-soft particles that experience significant scattering and too-hard particles that may not be sensitive to variations in the material of the pyramid. Accordingly, we explored the correlations between muon momentum and energy deposited in the rectangular scintillator strips, and this is outlined below. Concrete was omitted in all of these runs; E_μ here refers to the muon's energy before it reached the first detector plane.

Figure 65 depicts example results from two metrics for measuring energy absorption in the scintillator; on the left, muon hit multiplicity across all four detector planes, and on the right, total energy deposited across all planes for the same run. As expected, the latter is a Poisson distribution. It should be noted that the hit-multiplicity plot is shown on a log scale; it appears that a total of 4 hits per event - and therefore 1 hit per plane - is most common at this energy (E_μ = 40 GeV). This was discussed more thoroughly in section 6.1.

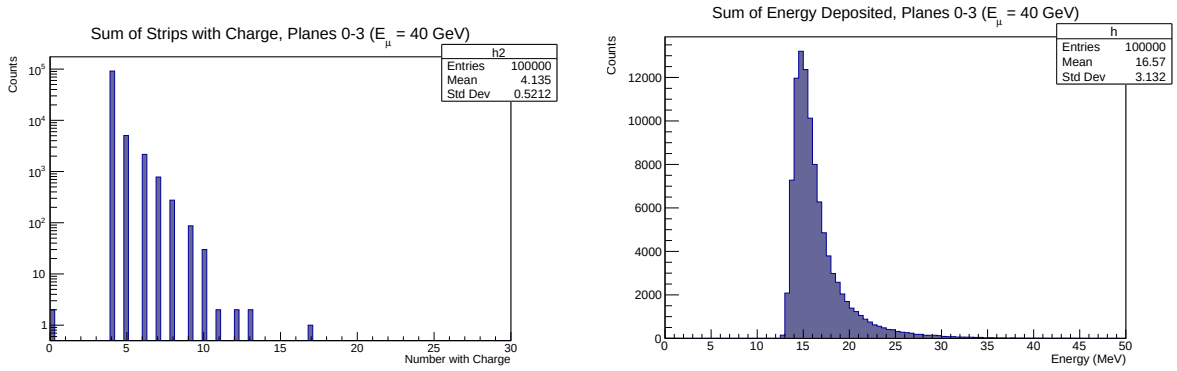

Figure 65: Left: distribution of total number of strips hit in all four detector planes after a run of 100,000 muons, with E_μ = 40 GeV. Right: distribution of total energy deposited in all four planes after the same run.

The left side of Figure 66 shows the mean total energy deposited in all four detector planes as a function of increasing incident muon energy; the right side of the figure shows the mean difference between incident and final muon energies as a function of the same. The latter plot demonstrates a noticeable increase in energy loss as E_μ increases. The former, on the other hand, shows very little absolute change over the range of momenta tested.

The energy collected by the detectors, then, does not vary measurably with the energy of the incident particle. Although the muons' overall energy loss is strongly correlated with their initial momenta, only a fraction of this lost energy is absorbed by the detectors. The remainder is lost to the surroundings, primarily by means of gamma rays, which unlike electrons do not strongly interact with the scintillator. It is worth noting that this effect is partially due to the small size of the detectors in the simulation; a larger array of detectors, like that filling an entire shipping container, would result in improved energy collection. However, this would likely not be enough to account for the discrepancy in Figure 76. So, before $\frac{dE}{dx}$ can be used to tag muons effectively, a way of increasing deposition in the detector planes is needed.

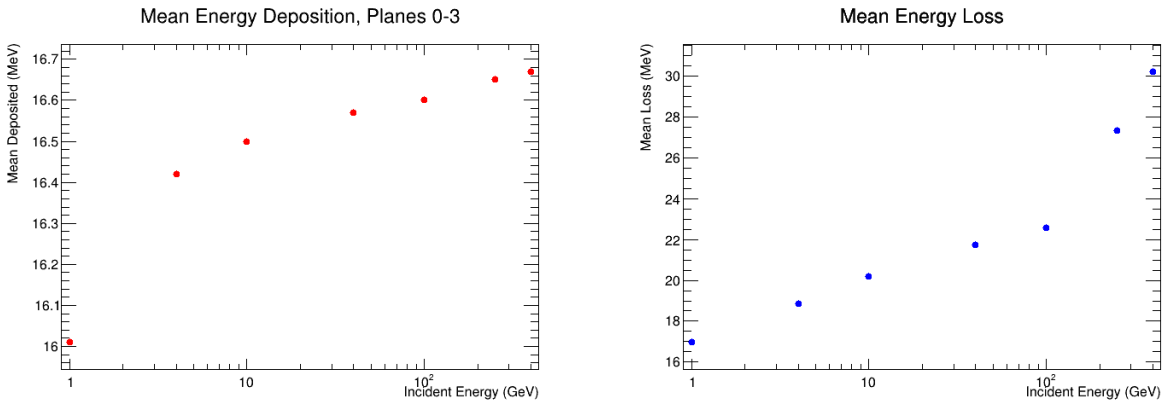

Figure 66: Left: the mean total energy deposited in all four scintillator planes as a function of incident muon energy. Right: the mean total energy lost by the muon as a function of incident energy. Particularly for muons at higher energies, there is a large discrepancy between this total energy loss and the energy deposited in the detectors themselves.

B.1.1 Basic Detector Design vs. Additional Pb Layer

To improve the correlation between incident muon momentum and energy deposition in the scintillators, we inserted a sheet of lead between detectors one and two (see Figure 67). The width and height of this sheet matched that of the detector planes; its thickness varied between 1 cm and 2 cm, while its exact placement ranged from 12 cm - 20 cm upstream of detector two. This addition was intended to result in a greater number of showers from secondary gamma rays and therefore an increased number of strips hit in the second detector. However, it had the potential disadvantage of degrading the detectors' position resolution.

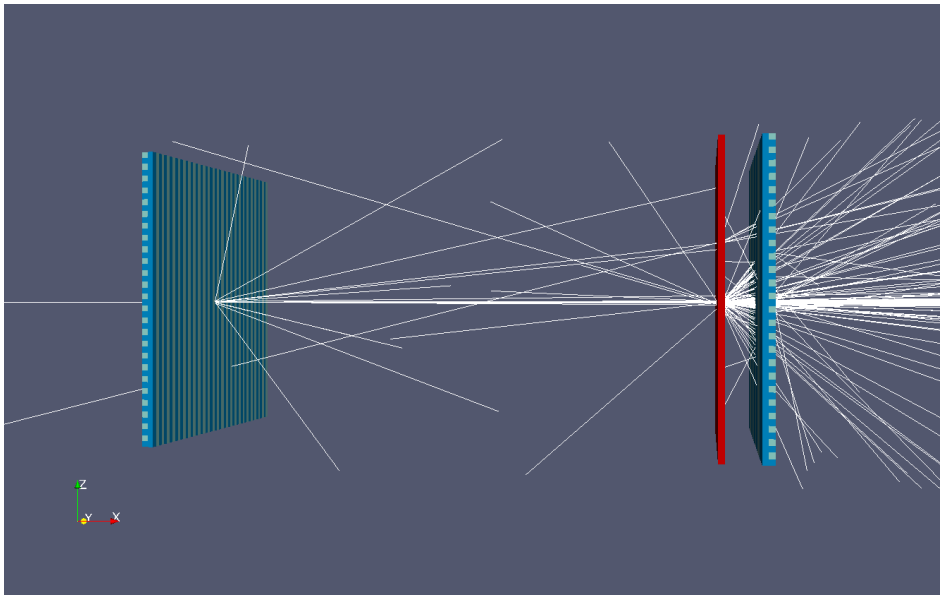

Figure 67: The modified detector design includes a lead sheet of varying thickness between the two detectors, and the placement of this sheet ranged from 12 cm - 20 cm upstream of detector 2. The goal of this addition was to increase the number of secondaries striking detector 2 without substantially degrading position resolution.

As shown in Figure 68, adding lead did have the intended effect of increasing hit multiplicity for higher-energy particles. The red data points represent the mean number of strips hit in detector two only for the original detector design (no Pb); the green and blue data represent the mean strips hit for configurations with 1 cm and 2 cm of lead, respectively. The lead sheets for both cases were placed 12 cm away from the detector. The correlation between E_μ and mean hit multiplicity is strongest for the 2-cm lead scenario.

However, these results also indicate that the modified detector design is likely unusable. The absolute increase in multiplicity over the range of energies tested is small (with a mean of c. 2.2 strips at $E_\mu = 1$ GeV and c. 3.2 strips at $E_\mu = 400$ GeV), and this range is itself larger than the probable real-life range of interest. Furthermore, the fraction of events that resulted in a substantially greater multiplicity is quite small. The plot on the left side of Figure 69 shows the percentage of events, out of a 10,000-event run, that yielded more than four strips hit in detector two as a function of increasing E_μ; the plot on the right shows the percentage of events that yielded more than ten hits. Here, the blue points correspond to the 1-cm Pb configuration, while the red points correspond to 2 cm Pb. Even at the highest energy simulated ($E_\mu = 400$ GeV), the fraction of events satisfying the four-strip condition does not exceed c. 12%, and the fraction satisfying the ten-strip condition does not exceed c. 3.5%. In short, adding a lead sheet between the two detectors is not a practical means of improving hit multiplicity for tagging incident E_μ. This design was not used in any of the other studies described in this paper.

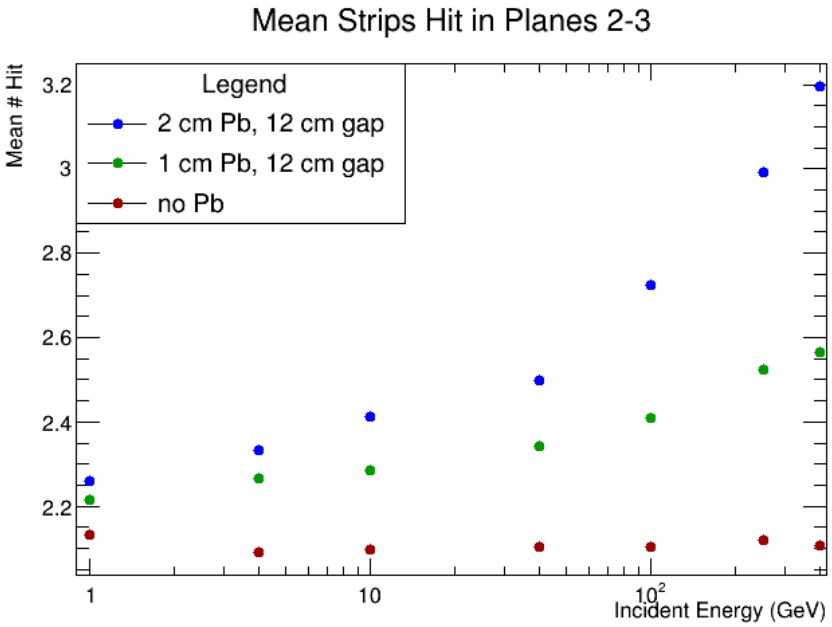

Figure 68: The mean number of strips hit in detector 2 as a function of incident muon energy, for various lead configurations; 10,000 muons per run.

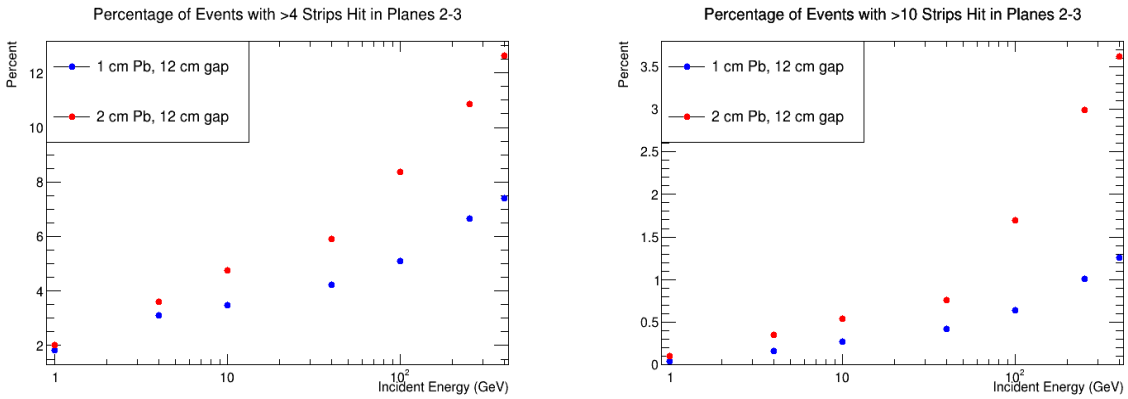

Figure 69: Out of 10,000 muons per run, the percentage of events for which more than 4 strips (left) or 10 strips (right) were hit in detector 2. Adding Pb yielded a strong correlation between incident muon energy and number of strips with charge, as hoped. However, this configuration is likely unusable.